



1 **A Sulfur Dioxide Covariance-Based Retrieval Algorithm**  
2 **(COBRA): application to TROPOMI reveals new emission**  
3 **sources**

4 **Nicolas Theys<sup>1</sup>, Vitali Fioletov<sup>2</sup>, Can Li<sup>3,4</sup>, Isabelle De Smedt<sup>1</sup>, Christophe Lerot<sup>1</sup>, Chris**  
5 **McLinden<sup>2</sup>, Nikolay Krotkov<sup>3</sup>, Debora Griffin<sup>2</sup>, Lieven Clarisse<sup>5</sup>, Pascal Hedelt<sup>6</sup>, Diego**  
6 **Loyola<sup>6</sup>, Thomas Wagner<sup>7</sup>, Vinod Kumar<sup>7</sup>, Antje Innes<sup>8</sup>, Roberto Ribas<sup>8</sup>, François**  
7 **Hendrick<sup>1</sup>, Jonas Vlietinck<sup>1</sup>, Hugues Brenot<sup>1</sup>, Michel Van Roozendael<sup>1</sup>**

8

9 <sup>1</sup> Royal Belgian Institute for Space Aeronomy (BIRA-IASB), Brussels, Belgium.

10 <sup>2</sup> Air Quality Research Division, Environment and Climate Change Canada, Toronto, Canada.

11 <sup>3</sup> Atmospheric Chemistry and Dynamics Laboratory, NASA Goddard Space Flight Center,  
12 Greenbelt, MD, USA.

13 <sup>4</sup> Earth System Science Interdisciplinary Center, University of Maryland, College Park, MD, USA.

14 <sup>5</sup> Université libre de Bruxelles (ULB), Spectroscopy, Quantum Chemistry and Atmospheric  
15 Remote Sensing (SQUARES), C. P. 160/09, Brussels, Belgium.

16 <sup>6</sup> Institut für Methodik der Fernerkundung (IMF), Deutsches Zentrum für Luft und Raumfahrt  
17 (DLR), Oberpfaffenhofen, Germany.

18 <sup>7</sup> Max Planck Institute for Chemistry (MPIC), Hahn-Meitner-Weg 1, 55128 Mainz, Germany.

19 <sup>8</sup> European Centre for Medium-Range Weather Forecast (ECMWF), Shinfield Park, Reading, RG2  
20 9AX, UK.

21

22 *Correspondence to:* N. Theys ([theys@aeronomie.be](mailto:theys@aeronomie.be) )

23

24

25

26

27

28



1

## 2 **ABSTRACT**

3 Sensitive and accurate detection of sulfur dioxide ( $\text{SO}_2$ ) from space is important for monitoring  
4 and estimating global sulfur emissions. Inspired by detection methods applied in the thermal  
5 infrared, we present here a new scheme to retrieve  $\text{SO}_2$  columns from satellite observations of  
6 ultraviolet back-scattered radiances. The retrieval is based on a measurement error covariance  
7 matrix to fully represent the  $\text{SO}_2$ -free radiance variability, so that the  $\text{SO}_2$  slant column density is  
8 the only retrieved parameter of the algorithm. We demonstrate this approach, named COBRA, on  
9 measurements from the TROPOspheric Monitoring Instrument (TROPOMI) aboard the Sentinel-  
10 5 Precursor (S-5P) satellite. We show that the method reduces significantly both the noise and  
11 biases present in the current TROPOMI operational DOAS  $\text{SO}_2$  retrievals. The performance of this  
12 technique is also benchmarked against that of the Principal Component Algorithm (PCA)  
13 approach. We find that the quality of the data is similar and even slightly better with the proposed  
14 COBRA approach. The ability of the algorithm to retrieve  $\text{SO}_2$  accurately is also further supported  
15 by comparison with ground-based observations. We illustrate the great sensitivity of the method  
16 with a high-resolution global  $\text{SO}_2$  map, considering two and a half years of TROPOMI data. In  
17 addition to the known sources, we detect many new  $\text{SO}_2$  emission hotspots worldwide. For the  
18 largest sources, we use the COBRA data to estimate  $\text{SO}_2$  emission rates. Results are comparable  
19 to other recently published TROPOMI-based  $\text{SO}_2$  emissions estimates, but the associated  
20 uncertainties are significantly lower than with the operational data. Next, for a limited number of  
21 weak sources, we demonstrate the potential of our data for quantifying  $\text{SO}_2$  emissions with a  
22 detection limit of about  $8 \text{ kt yr}^{-1}$ , a factor of 4 better than the emissions derived from the Ozone  
23 Monitoring Instrument (OMI). We anticipate that the systematic use of our TROPOMI COBRA  
24  $\text{SO}_2$  column data set at a global scale will allow identifying and quantifying missing sources, and  
25 help improving  $\text{SO}_2$  emission inventories.

26

## 27 **1. INTRODUCTION**

28 Sulfur dioxide ( $\text{SO}_2$ ) in the atmosphere rapidly oxidizes into sulfuric acid and sulfate aerosols,  
29 which have environmental effects ranging from local and long-range air pollution to global climate  
30 impact.  $\text{SO}_2$  is released into the atmosphere from anthropogenic activities, due to fossil fuel



1 burning (coal, oil and gas) and smelting, and from natural sources, mainly volcanoes. Satellites  
2 provide a viable means to monitor global SO<sub>2</sub> emissions and assess their environmental impacts.  
3 Since the late seventies, SO<sub>2</sub> vertical column densities (VCD) are provided by several ultraviolet  
4 (UV) polar-orbiting nadir instruments, namely the Total Ozone Monitoring Spectrometer (TOMS;  
5 Krueger, 1983), Global Ozone Monitoring Experiment (GOME; Eisinger and Burrows, 1998;  
6 Khokhar et al., 2005), SCanning Imaging Absorption spectroMeter for Atmospheric  
7 CHartographY (SCIAMACHY; Afe et al., 2004), Ozone Monitoring Instrument (OMI; Krotkov  
8 et al., 2006; Yang et al., 2007, 2010; Li et al., 2013; Theys et al., 2015), Global Ozone Monitoring  
9 Experiment-2 (GOME-2; Nowlan et al., 2011; Rix et al., 2012; Hörmann et al., 2013), Ozone  
10 Mapping and Profiler Suite (OMPS; Yang et al., 2013, Zhang et al., 2017) and TROPOspheric  
11 Monitoring Instrument (TROPOMI; Theys et al., 2017). From the various datasets, a remarkable  
12 trend emerges in the ability of successive sensors to detect weaker and more localized emissions.  
13 This is in part due to the better spatial resolution and signal-to-noise of the modern UV  
14 spectrometers (see e.g. Fioletov et al., 2013; Theys et al., 2019), but also from advances in retrieval  
15 techniques. In particular, the Principal Component Algorithm (PCA) applied to OMI (Li et al.,  
16 2013, 2020a) and OMPS (Zhang et al., 2017) proved to be a very efficient method to reduce  
17 retrieval noise and biases and thus to increase the sensitivity of the retrievals to weak SO<sub>2</sub>  
18 emissions to 30-40 kt yr<sup>-1</sup>. This enabled major improvements in bottom-up emissions inventories  
19 (Liu et al., 2018) and detection of missing SO<sub>2</sub> emission sources (Fioletov et al., 2016; McLinden  
20 et al., 2016).

21 TROPOMI, launched in October 2017 onboard the ESA and Copernicus Sentinel-5 Precursor (S-  
22 5P) platform, is the first atmospheric mission with a dedicated focus on the tropospheric  
23 composition (Veefkind et al., 2012). With a spatial resolution as good as 3.5 x 5.5 km<sup>2</sup> per ground  
24 pixel (3.5 x 7 km<sup>2</sup> before August 2019), it is specifically designed to monitor atmospheric  
25 constituents from urban to global scales. The first observations of SO<sub>2</sub> by TROPOMI were  
26 focusing on relatively large volcanic sources and indeed revealed the great potential of the  
27 instrument to inform about global volcanic SO<sub>2</sub> degassing with high resolution and unprecedented  
28 sensitivity (Theys et al., 2019; Queißer et al. 2019). However, further investigation of  
29 anthropogenic and volcanic SO<sub>2</sub> sources using TROPOMI revealed problems with the current  
30 TROPOMI SO<sub>2</sub> retrievals for weak emission sources (Fioletov et al., 2020). In brief, large-scale



1 and variable VCD biases on the order of 0.25 Dobson Unit (DU;  $1 \text{ DU} = 2.69 \times 10^{16} \text{ molecules cm}^{-2}$ ) are present in the data, which limits their use to medium to large  $\text{SO}_2$  sources only.

2

3 The operational TROPOMI  $\text{SO}_2$  algorithm is based on the Differential Optical Absorption

4 Spectroscopy technique (DOAS; Platt and Stutz, 2008), and essentially works in three steps

5 (details are given in Theys et al., 2017): a spectral analysis yielding  $\text{SO}_2$  slant column densities

6 (SCD), an empirical background correction of the SCDs and a radiative transfer calculation of air

7 mass factors (AMF) to convert the corrected SCD into the VCD output ( $\text{VCD} = \text{SCD}_{\text{cor}} / \text{AMF}$ ). As

8 a matter of fact, the  $\text{SO}_2$  SCD retrieval is subject to spectral misfits which can lead to systematic

9 offsets. These SCD errors are difficult to correct and arise from imperfect DOAS forward

10 modeling. Here, we propose an alternative spectral fitting approach, named COBRA, which

11 strongly reduces the  $\text{SO}_2$  SCD biases for the weak  $\text{SO}_2$  columns and suppresses the need for the

12 post-processing background correction. COBRA is akin to the PCA approach, which constitutes

13 the basis of the OMI and OMPS  $\text{SO}_2$  operational retrievals (Li et al., 2020b, 2020c). As

14 demonstrated below, COBRA significantly improves the quality as compared with the current

15 TROPOMI DOAS operational  $\text{SO}_2$  product. The analysis of two and a half years of data

16 oversampled at high resolution reveals many new  $\text{SO}_2$  emission sources globally, highlighting the

17 great performance of COBRA in terms of  $\text{SO}_2$  detection.

18 The paper is structured as follows. Section 2 describes the algorithm and its practical

19 implementation. In section 3,  $\text{SO}_2$  retrievals from COBRA are evaluated against other satellite data

20 sets, model results and ground-based observations. Section 4 presents long-term averaged global

21 results. In Section 5, we apply an emission inversion scheme to the COBRA  $\text{SO}_2$  data set and

22 compare with previously estimated  $\text{SO}_2$  emissions from the TROPOMI operational product. New

23  $\text{SO}_2$  emission sources detected by the COBRA are discussed. Conclusions are given in Section 6.

24

## 25 **2. METHODOLOGY**

### 26 **2.1 TROPOMI**

27 In this study, we use observations from the TROPOMI instrument on the Sentinel-5 Precursor

28 satellite. TROPOMI is a hyperspectral nadir sensor measuring solar radiation backscattered by the

29 atmosphere and reflected by the Earth, in the ultraviolet, visible, near-infrared and shortwave

30 infrared wavelength regions. TROPOMI delivers column amounts of minor atmospheric

31 constituents, such as  $\text{O}_3$ ,  $\text{NO}_2$ ,  $\text{SO}_2$ , HCHO, CO,  $\text{CH}_4$ , as well as aerosol and cloud information



1 (Veeffkind et al., 2012). The S-5P satellite is a polar orbiting platform crossing the equator at  
2 13:30h local time. A nearly global coverage is achieved in one day owing to a 2600 km wide  
3 swath. The footprint on the ground of the satellite measurement depends mainly on the across-  
4 track position in the swath and on the spectral band. For SO<sub>2</sub>, the ultraviolet spectral band 3 is  
5 used, and the swath is divided into 450 across-track positions (also referred to as ‘rows’). The  
6 spatial resolution for the center of the swath is approximately 3.5 x 7 km<sup>2</sup> (across-track x along-  
7 track) until 6 August 2019 when the sampling improved to 3.5 x 5.5 km<sup>2</sup>.

8 For this work, we analyze data measured between 1 April 2018 and 31 December 2020, and solar  
9 zenith angles (SZA) less than 60°.

## 10 2.2 Algorithm description

11 As mentioned above, the operational TROPOMI SO<sub>2</sub> algorithm is based on the DOAS technique,  
12 the most widely used method to derive atmospheric trace gas constituents in the UV-visible  
13 spectral range. The inverse problem can be expressed (employing the notation of Rodgers, 2000):

$$14 \quad y = K \cdot x + \epsilon \quad (1)$$

15 where  $y = -\log(I/I_o)$  is the optical depth, i.e. the logarithmic ratio of the wavelength calibrated  
16 measured intensity ( $I$ ) and the reference intensity spectrum ( $I_o$ ) over a given wavelength range,  $x$   
17 is the state vector including SCDs of relevant trace gases and closure fit parameters (e.g. for  
18 broadband effects),  $K$  is the forward model matrix with absorption cross-sections and other spectra,  
19 and  $\epsilon$  is the measurement noise. The solution can be approximated by least-square fitting:

$$20 \quad \hat{x} = (K^T S_\epsilon^{-1} K)^{-1} K^T S_\epsilon^{-1} y \quad (2)$$

21 where  $S_\epsilon$  is the measurement error covariance matrix. The latter matrix is most often taken diagonal  
22 (no error correlations) or proportional to unity (unweighted least-square). Eqs. (1) and (2) describe  
23 the simplest DOAS approach and are given here for illustration purpose only. In practice, the  
24 DOAS problem is fundamentally non-linear in many aspects and DOAS software packages, such  
25 as QDOAS (Danckaert et al., 2017), support different non-linear retrieval options (e.g. for  
26 wavelength shift and squeeze, or intensity offset), with the aim to improve the quality of the  
27 retrievals.

28 For weakly absorbing tropospheric species, retrieval artefacts are frequent with DOAS (notably  
29 for satellite nadir geometry), and are attributed to spectral interferences, imperfect forward model  
30 and incomplete treatment of instrumental effects (e.g., polarization sensitivity). For UV nadir SO<sub>2</sub>



1 retrievals in particular, biases in the data arise mainly from strong ozone absorption and imperfect  
2 treatment of the non-elastic Rotational Raman Scattering (Ring) effect. It is generally difficult to  
3 completely remove these offsets even after applying post-processing background corrections  
4 (Theys et al., 2017; Fioletov et al., 2020).

5 The Covariance-Based Retrieval Algorithm (COBRA) presented here, and illustrated for  
6 TROPOMI measurements, aims at correcting most of the artefacts in the DOAS SO<sub>2</sub> SCDs by  
7 optimally retrieving a single parameter: the SO<sub>2</sub> SCD.

8 First introduced by von Clarmann et al. (2001), the retrieval approach was developed by Walker  
9 et al. (2011) for nadir observations of SO<sub>2</sub> and NH<sub>3</sub> from the Infrared Atmospheric Sounding  
10 Interferometer (IASI). Then, the technique, also known as Hyperspectral Range Index (HRI), has  
11 been further refined and successfully applied to other trace gases and aerosols (e.g., Van Damme  
12 et al., 2014; Franco et al., 2018; Clarisse et al., 2019). The method proved to be very sensitive and  
13 led to superior data quality both in terms of precision and accuracy. Surprisingly, this technique  
14 has, to our knowledge, never been applied in the UV-visible spectral range.

15 Starting from Eq. 1, we assume the measurement vector can be linearized around a background  
16 SO<sub>2</sub>-free spectrum  $\bar{y}$ :

$$17 \quad y = \bar{y} + k \cdot SCD + \epsilon_{bg} + \epsilon \quad (3)$$

18 with  $\epsilon_{bg}$  being the uncertainty on the SO<sub>2</sub>-free spectrum, and  $\epsilon$  is the measurement noise. The SO<sub>2</sub>  
19 contribution to the measured spectral optical depth is approximated by the product of the  
20 instrument slit convolved absorption cross-section vector  $k$  (expressed in cm<sup>2</sup>/molecule) and the  
21 SO<sub>2</sub> slant column density  $SCD$  (in molecules/cm<sup>2</sup>). Here, we use as input of the retrieval the same  
22 SO<sub>2</sub> absorption cross-section data (Bogumil et al., 2003) as for the operational TROPOMI SO<sub>2</sub>  
23 retrievals (Theys et al., 2017), and the wavelength interval is 310.5 – 326 nm (see discussion  
24 below).

25 The basic principle of the method is to consider all contributions to the difference  $(y - \bar{y})$  other  
26 than SO<sub>2</sub> as an error term  $(\epsilon_{bg} + \epsilon)$  with a Gaussian distribution. If one can define an ensemble  $Y$   
27 of  $N$  measured spectra, representative of the total  $(\epsilon_{bg} + \epsilon)$  variability, and characterized by a mean  
28 measurement vector  $\bar{y}$  and a covariance matrix  $S$ :

$$29 \quad S = \frac{1}{N-1} \cdot \sum_{i=1}^N (y_i - \bar{y})(y_i - \bar{y})^T \quad (4)$$



1 then the solution of the problem writes as:

$$2 \quad \overline{SCD} = \overline{SCD} + (k^T S^{-1} k)^{-1} k^T S^{-1} (y - \bar{y}) \quad (5)$$

3 where  $\overline{SCD}$  is the mean SO<sub>2</sub> SCD of the ensemble ( $\overline{SCD} = 0$  by definition). It follows that the error  
4 on the retrieved SCD is given by:

$$5 \quad \overline{SCD}_{err} = \sqrt{(k^T S^{-1} k)^{-1}} \quad (6)$$

6 Fundamentally, COBRA generalizes the measurement error covariance matrix of Eq. 2 by  
7 incorporating geophysical background spectral variability (including all cross-correlations),  
8 variability from the atmosphere or induced by instrumental changes.

9 For spectra where no enhancements of SO<sub>2</sub> can be detected, the linearization (Eq. 3) simplifies to  
10  $y - \bar{y} = \epsilon_{bg} + \epsilon$  (7)

11 Both sides of the equation have therefore the same probability distribution, and it follows that the  
12 covariance matrix associated with  $\epsilon_{bg} + \epsilon$  can readily be constructed by applying Eq. 4 on a  
13 representative set of SO<sub>2</sub>-free spectra. The key is to define the ensemble  $Y$  such that  $y - \bar{y}$  cancels  
14 much of the systematic components of  $\epsilon_{bg}$ .

15 A remarkable feature of COBRA is its simplicity. The SO<sub>2</sub> SCD retrieval in Eq. 5 reduces to a  
16 simple dot product between the  $y - \bar{y}$  residue and  $k^T S^{-1}$  (skipping the normalization factor  
17  $(k^T S^{-1} k)^{-1}$ ). The vector  $k^T S^{-1}$  essentially contains the weights of each wavelength to the  
18 retrieved target column amount; the strength of the method relies in the fact that these weights are  
19 optimally determined by the measurements themselves. This is in contrast to the DOAS approach  
20 which mostly considers all wavelengths equal. Furthermore, DOAS also allows for cross-talks  
21 between the state vector elements, which can lead to an increase of the SCD data scatter (in  
22 particular for weak absorbers). This is obviously not the case for COBRA, as only a single  
23 parameter is retrieved, the SO<sub>2</sub> slant column. COBRA has other great advantages that we briefly  
24 outline here (read also Walker et al., 2011):

25 - The algorithm does not require a reference spectrum ( $I_o$ ). Indeed, equations 4 and 5 involve  
26 differences of logarithmic intensity ratios and thus  $I_o$  cancels out. Following the same logic,  
27 any constant spectral feature multiplicative to the radiance and shared by the ensemble  $Y$   
28 will have no influence on the retrieved SCDs.



- 1        - The COBRA results display low noise. This is a direct result of the COBRA approach in
- 2        that the wavelengths with the largest background radiance variability will have the lowest
- 3        weights on the retrieved SCD (Eq. 5).
- 4        - Very small biases are observed in the COBRA data (see next section). As a consequence,
- 5        an empirical SCD background correction is not needed.
- 6        - The approach works in principle for any wavelength range. This allows flexibility in case
- 7        of lower instrumental performance for certain wavelength regions.
- 8        - The covariance matrix  $S$  and mean measurement vector  $\bar{y}$  can be pre-calculated and the
- 9        implementation of COBRA then becomes very efficient in terms of processing time (about
- 10       an order of magnitude faster than DOAS non-linear schemes).

11 However, the practical implementation for COBRA require some caution. The main difficulty lies  
12 in the definition of the ensemble  $Y$  used to construct  $S$  (and  $\bar{y}$ ). The sample of  $N$  spectra should be  
13 highly representative of the measurement conditions under consideration, otherwise offsets in the  
14 SCDs will likely occur. Also, in principle, the spectra should be uncontaminated by absorption of  
15 the trace gas of interest. Finally,  $N$  should be large enough to insure statistically meaningful  
16 covariance results. For the retrieval of  $\text{SO}_2$  from TROPOMI, we have conducted a number of tests  
17 and come to the following implementation choices.

18 The input spectra for the covariance matrix calculation are analyzed separately for each TROPOMI  
19 row. We also treat each orbit individually to account best for the orbit-to-orbit variability. The data  
20 are first screened for solar zenith angles larger than  $60^\circ$ , and to cope with the latitudinal  
21 dependence, the data are divided into 6 equal and non-overlapping along-track segments. For each  
22 segment, an initial covariance matrix  $S$  is derived and initial estimates of  $\text{SO}_2$  SCDs are inverted  
23 through equation 5. In a second step, improved estimates of  $S$  and  $\text{SO}_2$  SCDs are obtained  
24 iteratively by removing  $\text{SO}_2$  contaminated spectra from the ensemble  $Y$ . To do this, we use the  
25 ratio of the  $\text{SO}_2$  SCD to its retrieval uncertainty (Eqs. 5 and 6), referred to as the signal to noise  
26 ratio (SNR):

$$27 \quad SNR = \frac{k^T S^{-1} \cdot (y - \bar{y})}{\sqrt{k^T S^{-1} k}} \quad (8)$$

28 A fixed SNR upper value of 1.5 is used for the filtering and the number of iterations is set to 4. A  
29 lower limit on the number  $N$  of  $\text{SO}_2$ -free spectra is set to 50. If this limit is reached, because of a





1 major volcanic eruption for example, the SO<sub>2</sub> SCD retrieval is entirely skipped for the  
2 corresponding row-segment pair.

3 It should be stressed that COBRA is close in concept to the PCA SO<sub>2</sub> algorithm of Li et al. (2013,  
4 2020a). In brief, the PCA scheme characterizes the background radiance variability using a number  
5 of leading PC spectra (typically 20-30), instead of a covariance matrix. The SO<sub>2</sub> column is then  
6 retrieved from the measured spectrum along with the PCs fitted parameters. In comparison,  
7 COBRA removes the need of having many parameters to fit. Only the SO<sub>2</sub> slant column density is  
8 determined and the background radiance variability is fully described by the covariance matrix. In  
9 a sense, COBRA can be considered as a generalization of the PCA scheme. It is therefore of great  
10 interest to compare the two methods (see section 3.1). Having this perspective in mind, we have  
11 made a number of choices to facilitate the comparison. For instance, we have used a spectral  
12 window from 310.5 to 326 nm (instead of 312-326 nm for the TROPOMI operational DOAS  
13 product), which includes the same strong SO<sub>2</sub> absorption bands as in the spectral range 310.5-340  
14 nm used by Li et al. (2013). This choice is also motivated by the inclusion of the intense absorption  
15 band at 310.8 nm which leads to a further reduction of the noise on the SO<sub>2</sub> column by about 25%.  
16 Note that initial tests with the TROPOMI operational algorithm using the 310.5-326 nm window  
17 were actually not very successful (large SO<sub>2</sub> SCD offsets). On the contrary, with COBRA, we  
18 tested both wavelength ranges (310.5-326 nm and 312-326 nm) and found only small differences  
19 between the retrieved SO<sub>2</sub> column patterns (Fig. S1).

20 In the following sections, SO<sub>2</sub> vertical columns will be presented. For the SCD to VCD conversion,  
21 we have used air mass factors from the operational product. Note that doing so is not strictly valid  
22 because one should expect lower AMFs due to the change in fitting window (from 310.5 to 326  
23 nm to 312-326 nm). To account for this, we have applied a constant scaling factor of 1.15 to the  
24 retrieved SO<sub>2</sub> VCDs. Based on radiative transfer calculations, we found this to be a good first order  
25 correction. However, in the future, AMFs shall be recalculated properly. For the cloud filtering  
26 and AMF cloud correction, the operational cloud product OCRA/ROCINN CRB is used (Loyola  
27 et al., 2018; Compernelle et al., 2020).

28 As a final note, it should be reminded that the operational TROPOMI algorithm also handles the  
29 retrieval of large SO<sub>2</sub> VCDs, by making use of multiple fitting windows (as described in Theys et  
30 al., 2017). In this study, we have not applied COBRA on the alternative fitting windows. While



1 there is no fundamental limitation to do so, COBRA is relevant mostly for low SO<sub>2</sub> columns. All  
2 the results presented in the next sections are for situations where the SO<sub>2</sub> VCDs are below 5 DU.

3

### 4 **3. VERIFICATION OF THE RETRIEVALS**

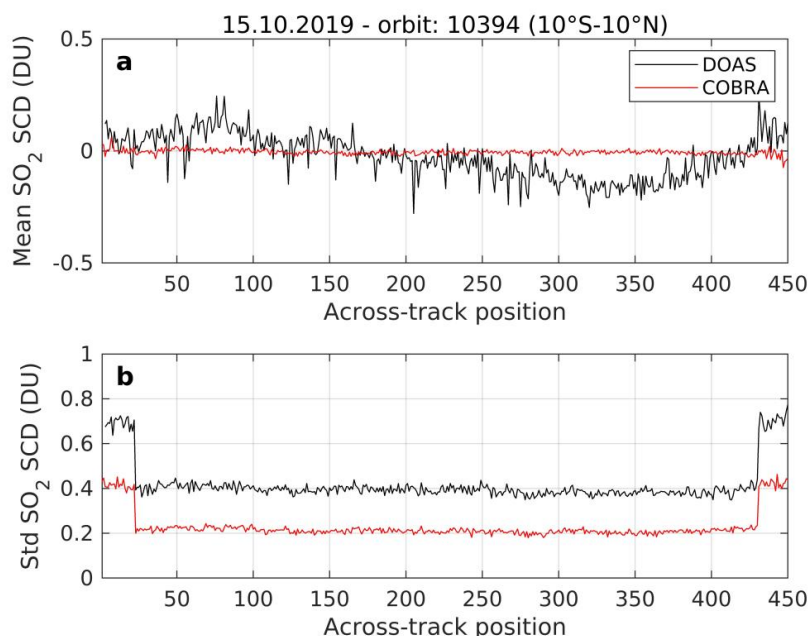
5

#### 6 **3.1 Comparison to satellite observations and CAMS**

7

8 In order to evaluate the SO<sub>2</sub> data from COBRA, it is interesting to first investigate the bias and  
9 data scatter over a clean region and compare with the operational product (hereafter referred to as  
10 ‘DOAS’). In Figure 1, the mean and standard deviation of SO<sub>2</sub> slant columns over an equatorial  
11 Pacific region are shown for one particular orbit, as a function of the TROPOMI row. As can be  
12 seen from Fig. 1a, the DOAS data suffer from SCD offsets in the range of  $\pm 0.25$  DU, despite the  
13 background correction applied. These offsets have a low-frequency dependence component with  
14 the across-track position but also vary sharply from one row to the next (leading to stripes in the  
15 SO<sub>2</sub> maps). In contrast, the COBRA results have very small SCD biases (mostly below  $\pm 0.025$   
16 DU) and no noticeable across-track dependence. It follows that COBRA is a very powerful bias  
17 self-correction and destriping scheme. In Fig. 1b, the standard deviations of the SO<sub>2</sub> SCD values  
18 are shown for both algorithms. Compared to DOAS, it is clear that the data scatter is significantly  
19 improved with COBRA, by a factor of 2. It is understood that part of this noise reduction is due to  
20 the change in fitting window (section 2.2), but most of the improvement (~75%) is from the  
21 COBRA approach. From Fig. 1, it is clear that the combined reduction of bias and data scatter  
22 provided by COBRA over the DOAS results is very significant. From a practical point of view, a  
23 factor of 2 improvement of the data scatter means 4 times less pixels to average to reach a certain  
24 noise level.

25 In Fig. 1b, we note also a distinct increase in data scatter for the outermost rows, for both DOAS  
26 and COBRA. This feature is due to difference in detector signal binning at the swath edges which  
27 leads to an increase in radiance shot noise. To keep the data of the best quality, we will not use the  
28 50 outermost rows in the following of the paper.



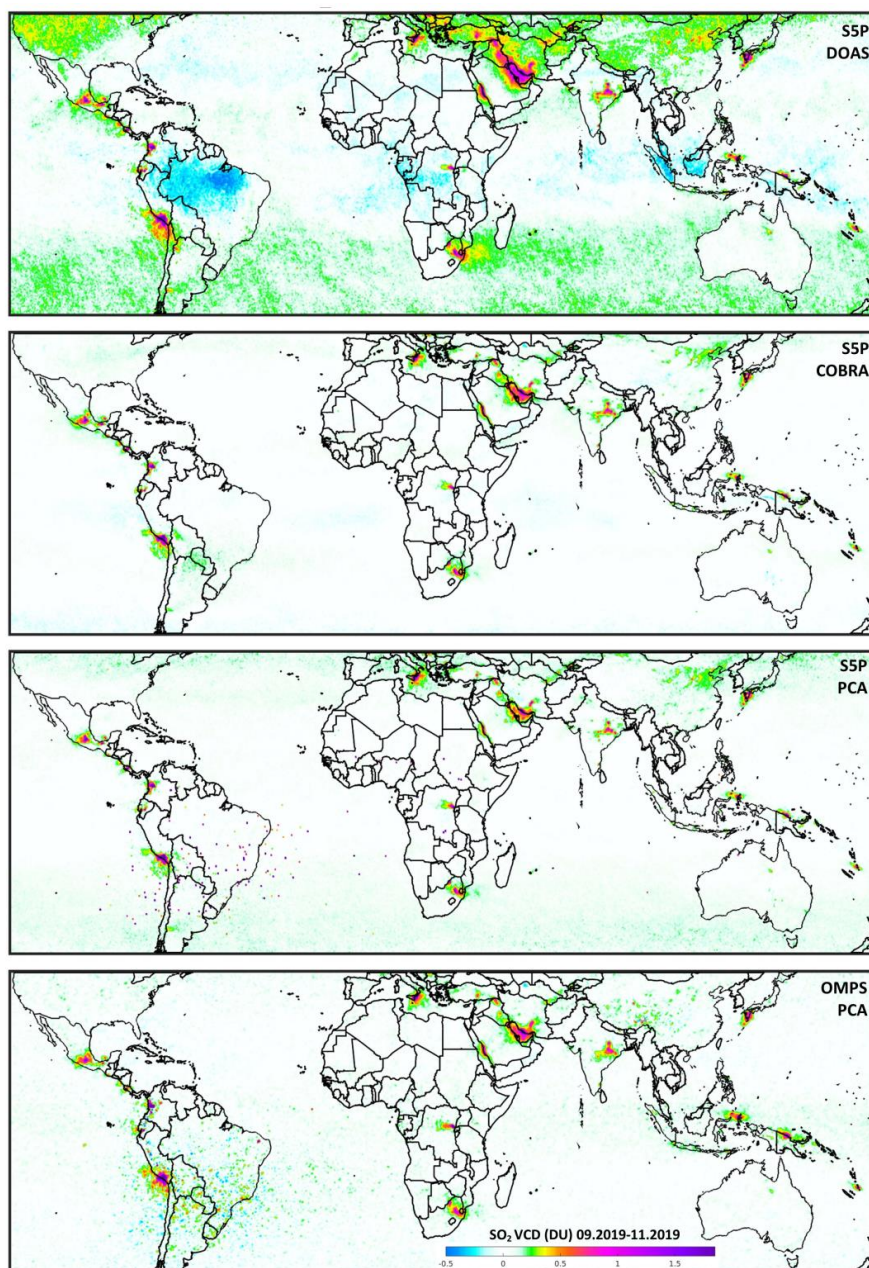
1  
2 Figure 1. (a) Mean SO<sub>2</sub> slant columns from (black) DOAS (background corrected) and (red)  
3 COBRA for one orbit (10394 on 15 October 2019) over the equatorial Pacific region (10°S-10°N),  
4 as a function of the across-track position of TROPOMI, (b) same as (a) for the SO<sub>2</sub> SCD standard  
5 deviation.

6  
7 Figure 2 compares the DOAS and COBRA seasonal averaged SO<sub>2</sub> VCD maps from September to  
8 November 2019. The data are gridded at a resolution of 0.1° x 0.1° and smoothed by a 2-  
9 dimensional 5-points box car function. Both DOAS and COBRA results are extracted using  
10 identical pixel selection criteria: SZA less than 60°, radiometric cloud fraction lower than 30% and  
11 TROPOMI rows 26-424. From Fig. 2, several artefacts are evident in the DOAS product. Negative  
12 values are found in the tropics and a large scale positive bias at mid-latitudes. In comparison,  
13 COBRA remarkably solves all the systematic biases found in the operational product whereas the  
14 signal from major SO<sub>2</sub> sources (e.g. in China, India, Middle-East, South Africa, Central and South  
15 America) is nicely preserved. Note that for individual pixels with unambiguous detection of SO<sub>2</sub>  
16 (typically SO<sub>2</sub> VCDs larger than 2 DU), the agreement between DOAS and COBRA is excellent  
17 (see e.g., Fig. S2). In Fig. 2, a closer look at the COBRA SO<sub>2</sub> map still reveals some negative  
18 values for specific locations. For instance, the Garabogazköl Basin near the Caspian Sea is



1 particularly visible. It is characterized by a salt flat with a high albedo. This surface effect is  
2 apparently poorly represented in the radiance covariance, and leads to the negative values observed  
3 in the data.

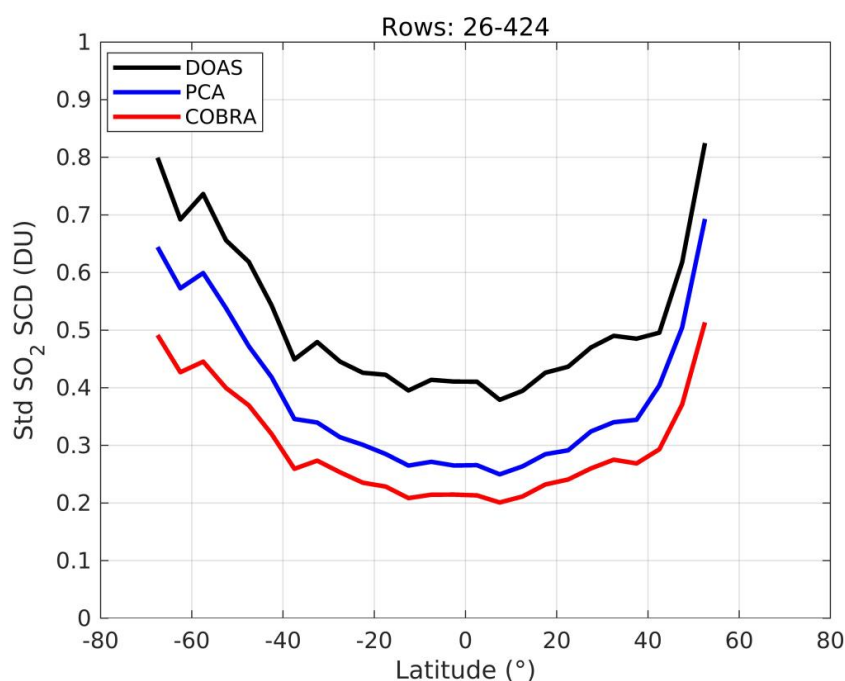
4 Retrieval results using the new COBRA are also evaluated in Fig. 2 against a scientific TROPOMI  
5 SO<sub>2</sub> product generated using the PCA approach. The settings of the experimental TROPOMI PCA  
6 SO<sub>2</sub> algorithm, including the spectral range and number of iterations, are identical to the  
7 operational OMI algorithm with the following exceptions: 1) TROPOMI pixels from each row are  
8 grouped into sectors of 20-degree latitude bands, instead of three sectors as in the OMI algorithm;  
9 2) a third degree polynomial is removed from each Sun-normalized radiance spectrum before PCA  
10 analysis; 3) at maximum 20 PCs are used in the fitting instead of 30 in the current OMI algorithm  
11 (Li et al., 2020a); and 4) no attempts were made to reduce TROPOMI retrieval noise over the SAA  
12 affected areas. For this exercise, the PCA scheme uses as input the same SO<sub>2</sub> absorption cross-  
13 section data (Bogumil et al., 2003) as for the DOAS and COBRA retrievals, and the same selection  
14 of pixels. Figure 2 also compares the TROPOMI SO<sub>2</sub> columns (from DOAS, COBRA and PCA)  
15 to the operational OMPS SO<sub>2</sub> PCA retrievals NMSO2\_PCA\_L2 V2 (Zhang et al., 2017; Li et al.,  
16 2020c). Although OMPS has a coarser resolution (50 x 50 km<sup>2</sup>) than TROPOMI, it provides  
17 nonetheless a useful reference data because it operates on the Suomi National Polar-orbiting  
18 Partnership (SNPP) satellite which flies in loose formation with S-5P (i.e. 3-5 minutes difference  
19 of overpass time). To allow a meaningful comparison, the OMPS pixels were selected similarly as  
20 TROPOMI, i.e. with cloud radiance fraction lower than 30% and OMPS across-track positions 3-  
21 34. Note finally that to avoid discrepancies due to different a-priori profiles in the TROPOMI and  
22 OMPS retrievals, a fixed AMF of 0.4 was used for all four data sets. As can be seen from Fig.2,  
23 an overall excellent agreement is found between COBRA and PCA retrievals, the observed SO<sub>2</sub>  
24 spatial distributions being essentially the same. However, the OMPS SO<sub>2</sub> data set has different  
25 patterns over China (possibly due to sampling differences), and also appears noisier than the  
26 TROPOMI results (as expected from the smaller number of pixels). When comparing the  
27 TROPOMI COBRA and PCA maps, very consistent results are found. Yet, the quality of COBRA  
28 seems slightly better than the PCA retrievals. In particular, COBRA is much less sensitive to the  
29 South Atlantic Anomaly than PCA data, which exhibit many outliers in the corresponding region.  
30 At mid-latitudes, there is also a slight positive bias (of about +0.1 DU on average) and higher noise  
31 in the PCA results compared to COBRA.



1  
2 Figure 2. Comparison of seasonal mean SO<sub>2</sub> columns for September to November 2019 retrieved  
3 from TROPOMI DOAS, COBRA, PCA and OMPS PCA algorithms (from top to bottom).  
4 Consistent pixel selection criteria, gridding and retrieval settings are applied (see text). For all four  
5 data sets, a fixed AMF of 0.4 is applied.



1 We have estimated the data scatter for the three TROPOMI data sets, based on measurements from  
2 the same orbit over the Pacific as Fig. 1. Results are shown in Figure 3, as a function of latitude.  
3 We find that COBRA has a SCD noise level 20-25% lower than the PCA retrievals, and twice  
4 better than DOAS (as in Fig. 1). Translating the numbers of Figure 3 in terms of vertical columns  
5 for a typical pollution scenario, we estimate the retrieval precision for individual pixels typically  
6 to be 0.5 - 1 DU for COBRA.



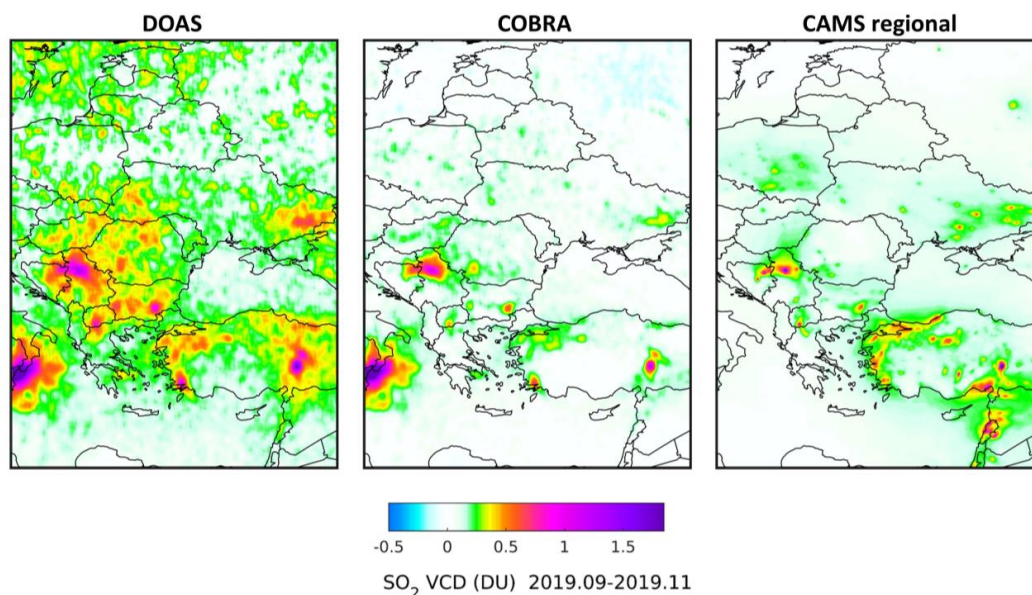
7  
8  
9 Figure 3. Standard deviation of the SO<sub>2</sub> slant columns as retrieved from DOAS (black), PCA (blue)  
10 and COBRA (red) for one TROPOMI orbit (10394 on 15 October 2019, same as Fig. 1) for rows  
11 26-424, as a function of latitude (for 5° bins).

12 To further evaluate the overall quality of the COBRA retrievals, the SO<sub>2</sub> VCDs can also be  
13 compared to model data. Here, we have used the output of the Copernicus Atmosphere Monitoring  
14 Service (CAMS; <https://atmosphere.copernicus.eu/>) regional model, for September to November  
15 2019. The CAMS regional air quality production is based on an ensemble of 9 European air quality  
16 models that are run at a resolution of 0.1° and produce 4-day, daily forecasts of the main  
17 atmospheric pollutants, including SO<sub>2</sub>. The forecasts and analyses from all 9 models are combined



1 in calculating the median value of the individual outputs, which is designated as the ENSEMBLE  
2 output and is the field used in this study. The CAMS regional ensemble data was obtained from  
3 the Copernicus Atmosphere Data Store (ADS, <https://atmosphere.copernicus.eu/data>). More  
4 information about the CAMS regional system can be found on the ECMWF website  
5 (<https://confluence.ecmwf.int/display/CKB/CAMS+Regional:+European+air+quality+analysis+and+forecast+data+documentation>).  
6 The CAMS regional system used the CAMS-REG-  
7 AP\_v2\_2\_1 emissions (reference year: 2015) between June 2019 and February 2020, and the  
8 updated CAMS-REG-AP\_v3\_1 emissions dataset (reference year: 2016) since February 2020.

9 In Figure 4, seasonal regional maps of S-5P SO<sub>2</sub> VCDs over Eastern Europe from the DOAS and  
10 COBRA schemes are compared to the output of the CAMS regional model, for September to  
11 November 2019. From the maps, it is clear that the COBRA results are in much better agreement  
12 with the CAMS analysis than the DOAS data. Owing to the quasi-absence of bias and the low  
13 noise level, the COBRA data allows better isolation of the emission sources. The agreement  
14 between COBRA and CAMS is however not perfect and there are several explanations for this.  
15 Most of the SO<sub>2</sub> emissions in this region are from coal-fired power plants and the emission  
16 inventory used by CAMS is likely not reflecting neither the actual activity nor the emission  
17 mitigation solution (e.g. SO<sub>2</sub> scrubbers) at each power plant. Noteworthy is also the absence of  
18 SO<sub>2</sub> emissions from Mt. Etna in CAMS. Secondly, the AMFs used here are calculated with SO<sub>2</sub>  
19 profiles from TM5, a different model with a coarser resolution (1° x 1°) than CAMS regional.  
20 Therefore the COBRA and CAMS SO<sub>2</sub> columns cannot be strictly compared. Nevertheless, the  
21 comparison in Fig. 4 is encouraging. In the future, the COBRA SO<sub>2</sub> retrievals together with the  
22 corresponding column averaging kernels (Eskes and Boersma, 2003) could be ingested in the  
23 CAMS assimilation system to better constrain the model SO<sub>2</sub> output and emission estimates.



1  
2 Figure 4. Seasonal mean  $\text{SO}_2$  columns for September to November 2019 from (left-center)  
3 TROPOMI DOAS and COBRA retrievals, and (right) simulated by the CAMS regional model.  
4 The CAMS data are displayed at the  $0.1^\circ \times 0.1^\circ$  native resolution.

### 5 3.2 Comparison to ground-based MAX-DOAS observations

6  
7 The Multi-Axis DOAS (MAX-DOAS) measurement technique is an established method to retrieve  
8 tropospheric trace gas columns and vertical profiles from a sequence of spectral observations  
9 performed at various elevation angles above the horizon (Hönninger and Platt, 2002; Tirpitz et al.,  
10 2021). MAX-DOAS measurements leverage the fact that low elevation measurements have  
11 enhanced sensitivity to atmospheric pollutants in the boundary layer and that the combination of  
12 the different elevations carries information on the vertical distribution of the trace gas of interest  
13 as well as aerosols. The simplest estimation of the tropospheric VCD from MAX-DOAS  
14 measurements is obtained by scaling the differential SCD at a given elevation angle (often  $15^\circ$  or  
15  $30^\circ$ ) with an AMF assuming a geometrical light path through the trace gas layer. Recently, more  
16 sophisticated approaches have been developed to retrieve the concentration profile in the  
17 troposphere using multiple elevation measurements.  
18 Here we compare our TROPOMI  $\text{SO}_2$  VCD data to MAX-DOAS observations at two sites, both  
19 characterized by relatively low  $\text{SO}_2$  columns: Xianghe and Mohali (Table 1). In general, the





1 different MAX-DOAS instruments and SO<sub>2</sub> retrievals share common characteristics, practices and  
2 approaches, and the reader is referred to the publications listed in Table 1 for more detailed  
3 information.

4 For the comparison, we have used a common set of selection criteria for the satellite data. For each  
5 day, we selected the TROPOMI pixels within a 25 km radius circle around the station of interest,  
6 a strict radiometric cloud fraction threshold of 20%, SZA lower than 60° and AMF larger than 0.2.  
7 If the number of retained pixels is larger than 10 then the mean SO<sub>2</sub> VCD is calculated and  
8 compared to the averaged SO<sub>2</sub> column for the MAX-DOAS measurements within ±1 hour of the  
9 S-5P overpass time.

10 Regarding the ground-based retrievals, the SO<sub>2</sub> VCDs are estimated, for Mohali, using the 15°  
11 elevation SO<sub>2</sub> SCDs and geometrical AMFs. Conversely, the retrieved data for Xianghe consist of  
12 SO<sub>2</sub> profiles. These are integrated along the vertical to provide the VCDs. Moreover, to make the  
13 comparison between MAX-DOAS and TROPOMI more consistent, we have rescaled the  
14 TROPOMI VCDs using the satellite averaging kernels (Eskes and Boersma, 2003) and the MAX-  
15 DOAS SO<sub>2</sub> profiles at Xianghe.

16

17 Table 1. Summary of SO<sub>2</sub> VCDs comparison

18

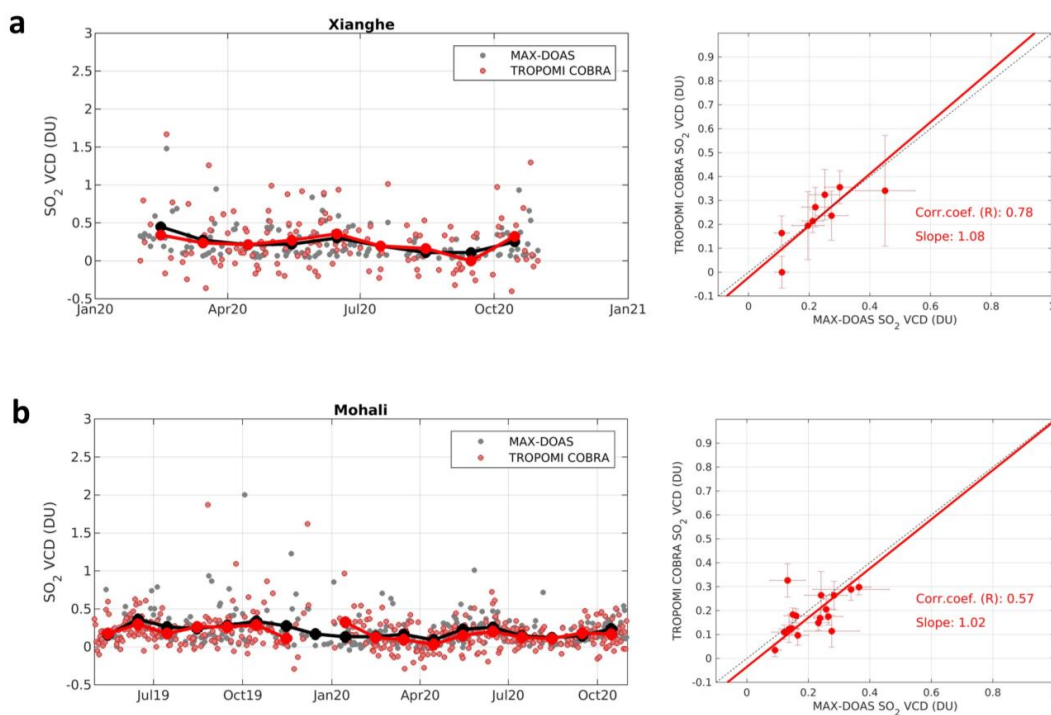
Station	Reference	MAX-DOAS VCD calculation	Period	Mean SO <sub>2</sub> VCD (DU) for SZA < 50° (50° < SZA < 60°)		
				MAX- DOAS	S-5P COBRA	S-5P DOAS
Xianghe, China 39.77°N 117°E	Wang et al. (2014)	Integrated profile	01.2020- 10.2020	0.2 (0.28)	0.21 (0.34)	0.34 (0.77)
Mohali, India 30.67°N 76.74°E	Kumar et al. (2020)	15° elevation (geometrical)	05.2019- 10.2020	0.21 (0.18)	0.18 (0.26)	0.16 (0.50)

19

20 The comparison results between COBRA and MAX-DOAS measurements are shown in Figure 5a  
21 and 5b, for Xianghe and Mohali, respectively. Overall, the agreement between COBRA and MAX-  
22 DOAS data is very good, keeping in mind that the levels of SO<sub>2</sub> columns are quite low. The slopes  
23 of the regression lines are close to unity. In Table 1, the mean SO<sub>2</sub> columns from MAX-DOAS,  
24 TROPOMI COBRA and DOAS retrievals are given at each station and for different SZAs. A  
25 striking feature of the comparison is that the COBRA results show similar good agreements over



1 a wide range of SZA. It further supports the idea that COBRA yields unbiased results over varying  
2 observation conditions. This is in contrast to the DOAS product which is clearly biased high for  
3 high SZA.



4  
5 Figure 5. (left) Comparison of monthly mean SO<sub>2</sub> columns from MAX-DOAS and TROPOMI  
6 COBRA for (a) Xianghe, and (b) Mohali. The grey and pale red dots correspond to the individual  
7 days. (right) Scatter plots of monthly mean SO<sub>2</sub> columns of TROPOMI COBRA vs MAX-DOAS  
8 observations. Error bars are the standard errors on the monthly average SO<sub>2</sub> columns. The  
9 correlation coefficient and slope of the regression line are given as an inset for each plot.

10

#### 11 4. GLOBAL RESULTS

12

13 In this section, we present long-term global results from COBRA, based on two and a half years  
14 (April 2018 – December 2020) of cloud-free TROPOMI data (radiometric cloud fraction less than  
15 30%). Using an oversampling technique, a global average SO<sub>2</sub> column map at 0.015° x 0.015°  
16 resolution was obtained and smoothed by a 2-dimensional 10-points box car function. Figure 6  
17 shows the resulting SO<sub>2</sub> distribution for specific regions, over East China, India, the Middle East,



1 South America, South Africa, US and Europe (the global map is also available in the form of a  
2 Google Earth /geotiff file, as supplementary material). Figure 6 also shows the locations of the  
3 SO<sub>2</sub> sources based on the latest OMI 2005-2019 catalogue (Fioletov et al., 2016), with a total of  
4 588 sites, including power plants, smelters, oil and gas industry sources, and volcanoes. As can be  
5 seen, many of the sources of the catalogue are easily identified as SO<sub>2</sub> hotspots on the map.  
6 Conversely, there is also a significant number of sources in the inventory with no detectable SO<sub>2</sub>  
7 in the TROPOMI data, but one should keep in mind that the catalogue gathers emission sources  
8 since the beginning of the OMI data record in 2005 and several of these sources have ceased  
9 operations or decreased drastically their emissions since then (e.g. due to the operation of SO<sub>2</sub>  
10 scrubbers in coal power plants). To help identifying those sources, Figure 6 shows with a different  
11 marker the sources detected by OMI for 2018-2019 (i.e. the sources with emissions above the  
12 detection limit, as in Fioletov et al. (2016) and McLinden et al. (2016); see also Section 5.2). This  
13 is also helpful to highlight the differences in sensitivity, as many sources are detected by  
14 TROPOMI but not by OMI.

15 Generally speaking, the SO<sub>2</sub> maps of Figure 6 are very detailed. Biases over clean regions are  
16 remarkably low, and emissions-related patterns with SO<sub>2</sub> VCDs less than 0.25 DU are clearly  
17 visible in many places. By scrutinizing the SO<sub>2</sub> distributions, one can identify numerous sources  
18 from the current catalogue but also several potentially new source regions. However, some care  
19 must be taken in attributing new sources and relate this to the improved sensitivity of TROPOMI  
20 COBRA. First, the catalogue is arguably not resolving well the individual sources for dense  
21 regions (e.g., in East China and India) and, as a matter of fact, typically reports a total emission  
22 estimate of a point-like source for what is in reality a cluster of sources. While the algorithm to  
23 handle such clusters of sources exists (Fioletov et al., 2017), it has not been implemented in the  
24 catalogue yet. Second, the SO<sub>2</sub> catalogue is being populated on a best-effort basis, and a number  
25 of emission sources might be missing, in particular for emerging countries where industrial  
26 infrastructures are built quickly. Third, SO<sub>2</sub> outflow from the strong sources - or clusters of sources  
27 - can lead to variations in the map and thus fictitious emission sources. Finally, retrieval artefacts,  
28 measurement noise or sampling related issues can also lead to false sources identification. Note  
29 that a comprehensive identification and classification of new sources from the COBRA SO<sub>2</sub> data  
30 is not the scope of the present study. Here, we aim at discussing plausible new SO<sub>2</sub> sources (i.e.

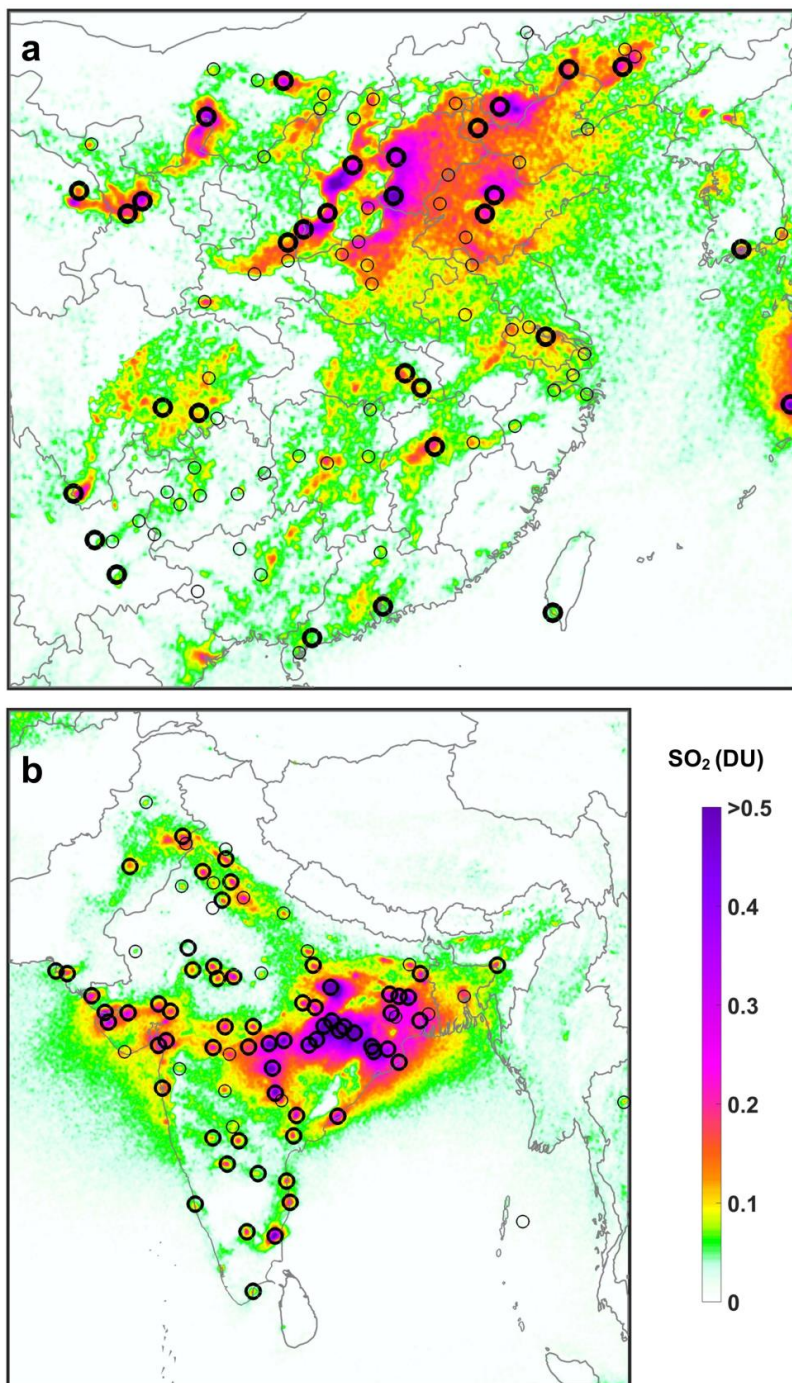


1 not in the OMI catalogue). In Section 5.2, we will further demonstrate the excellent performance  
2 of COBRA to detect very weak emissions, for a limited number of sources.  
3 The new identified sources are characterized by low SO<sub>2</sub> column levels in the range 0.05 - 0.2 DU.  
4 For instance, in Fig. 6a we observe hotspots of SO<sub>2</sub> from power plants (mostly coal but also likely  
5 gas) in North- and South-Korea, northern Vietnam (near Haiphong), several Chinese provinces  
6 (e.g., Hubei, Guangxi, Guangdong) and along the coast of China. In Fig. 6b, several weak emission  
7 sources can be isolated in India (e.g., over the western coast and the Indo-Gangetic plain), Pakistan,  
8 Bangladesh and Sri Lanka (near the city of Colombo). In the Middle East (Fig. 6c), most of the  
9 SO<sub>2</sub> emissions are from oil and gas related industries, like power plants, gas flaring and refineries.  
10 Examples of weak SO<sub>2</sub> emissions can be found in Saudi Arabia, Oman, Egypt, Syria (near the city  
11 of Damascus) and Iran. In South America (Fig. 6d), new emission sources are popping up, notably,  
12 in Brazil (near Rio de Janeiro, São Paulo and Porto Alegre), and on both sides of the Andes (in  
13 Chile and Argentina). In South Africa (Fig. 6e), in addition to the strong emissions from the coal  
14 power plants of the Highveld, a clear SO<sub>2</sub> signal is detected over Cape town. Interestingly, the  
15 measured SO<sub>2</sub> distribution nicely matches the orography setting. In the US (Fig. 6f), the most  
16 striking emission region is the state of California, with enhanced SO<sub>2</sub> over the Central Valley and  
17 the city of Los Angeles. Over the central and eastern parts of the US, the emissions from power  
18 plants have declined dramatically over the last 15 years (Krotkov et al., 2016). However, the data  
19 still show enhanced SO<sub>2</sub> over some of them. In Europe (Fig. 6g), most of the observed enhanced  
20 SO<sub>2</sub> correspond to sources already in the catalogue. Still, a number of small spots are found e.g.,  
21 in eastern Europe (Romania, Serbia, Kosovo, Hungary), Germany (near Leipzig), Turkey and  
22 Tunisia (Gulf of Gabes). Interestingly, enhanced SO<sub>2</sub> is also observed over the Gibraltar strait and  
23 Red sea which might result from shipping emissions.  
24 Overall, the SO<sub>2</sub> maps of Fig. 6 nicely illustrate the great ability of TROPOMI to detect weak SO<sub>2</sub>  
25 point emissions sources when analyzed using a sensitive approach as COBRA. Using Google Earth  
26 imagery and information on industrial facilities location, we were able to confirm that many  
27 features in the SO<sub>2</sub> map are real sources. For this, we have also compared our SO<sub>2</sub> data to  
28 tropospheric NO<sub>2</sub> column maps from TROPOMI. An example of comparison is shown in Fig. S3  
29 for a region over Central Asia. There, the SO<sub>2</sub> emissions sources in the catalogue are mostly from  
30 coal power plants and smelters, in the Xinjiang province (China) and east Kazakhstan. As can be



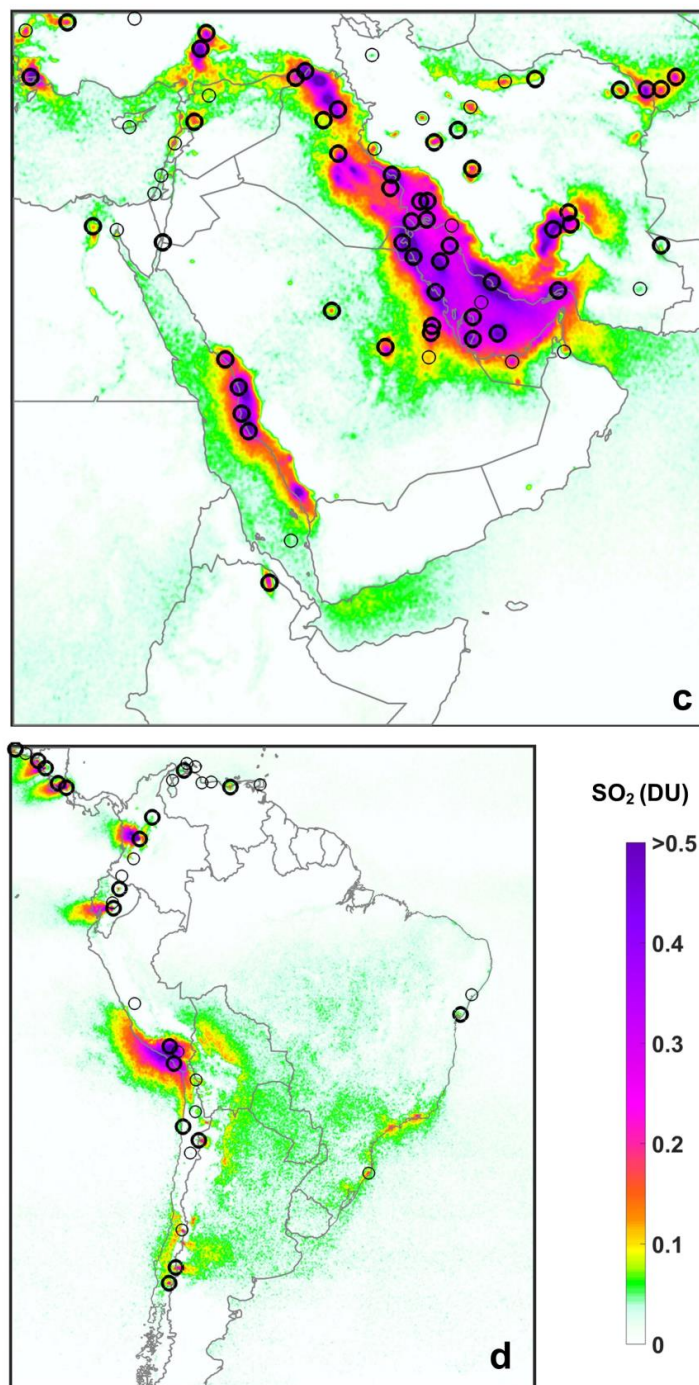
1 seen in Fig. S3, several other SO<sub>2</sub> emission hotspots are detected (notably in the Xinjiang province)  
2 which clearly coincide with locations with enhanced tropospheric NO<sub>2</sub>.  
3 Nevertheless, several patterns in the SO<sub>2</sub> map (Fig. 6) are hard to relate to point source emissions.  
4 In particular, the SO<sub>2</sub> signal observed over Cape town (Fig. 6e) and Los Angeles (Fig. 6f) could be  
5 due to area sources rather than point emissions. Over South America (Fig. 6d) and eastern US (Fig.  
6 6f), the apparent SO<sub>2</sub> background is intriguing. It is unclear whether this could be due to real SO<sub>2</sub>  
7 emissions or not. We also identify several artefacts in the data. Unsurprisingly, biases in the data  
8 occur for specific conditions which are under-sampled or not optimally represented by the  
9 covariance matrix. These are most often surface-related effects (due to peculiar albedo or elevated  
10 terrain). One illustration of this problem is given in Fig. 6c, over the Nile Valley. Although some  
11 real SO<sub>2</sub> emissions are found in the area, with SO<sub>2</sub> VCDs larger than ~0.1 DU, there are also  
12 unexpected enhancements in the SO<sub>2</sub> column that follow the Nile River. These are probably due  
13 to the very dark surfaces there. Similarly, elevated values are also found further South in Sudan  
14 and Ethiopia, over vegetated scenes. However, the resulting SO<sub>2</sub> VCD biases are overall very  
15 small, typically less than 0.04 DU (~ 1 x 10<sup>15</sup> molecules/cm<sup>2</sup>), and can be suppressed by a local  
16 bias correction or more sophisticated approaches.

17 As mentioned above, the attribution of new sources based on SO<sub>2</sub> maps is not straightforward.  
18 Efficient space-based techniques do exist, to isolate sources and estimate their emissions (Fioletov  
19 et al., 2015; McLinden et al., 2016; Clarisse et al., 2019). However, applying such methods  
20 systematically to the TROPOMI COBRA SO<sub>2</sub> data goes beyond the scope of this paper. Instead,  
21 in the next section, we will estimate the SO<sub>2</sub> emissions for the known largest sources, and  
22 demonstrate the potential of COBRA for the retrieval of weak emissions, for a limited number of  
23 new sites.



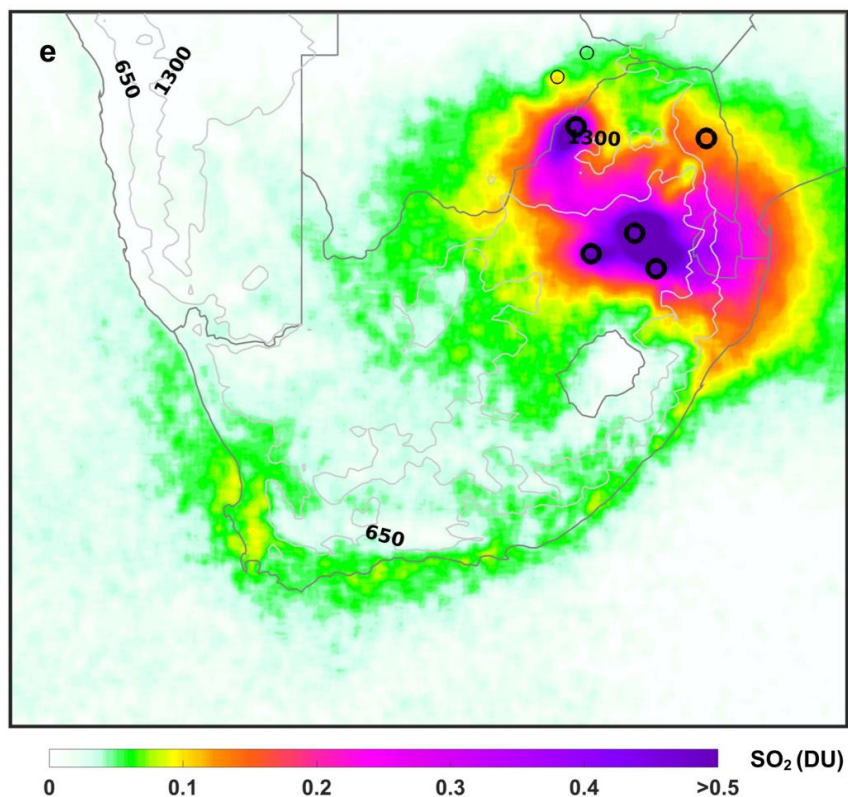


- 1 Figure 6. Averaged SO<sub>2</sub> column (in DU) for April 2018 to December 2020 over (a) East China, (b)
- 2 India, (c) the Middle East, (d) South America, (e) South Africa, (f) US and (g) Europe. The black
- 3 circles mark the locations of SO<sub>2</sub> sources detected by OMI (in bold for the 2018-2019 period, see
- 4 text). Due to the massive eruption of Raikoke on 21 June 2019, all data in the northern hemisphere,
- 5 for the 3 months period after the eruption, are filtered out.



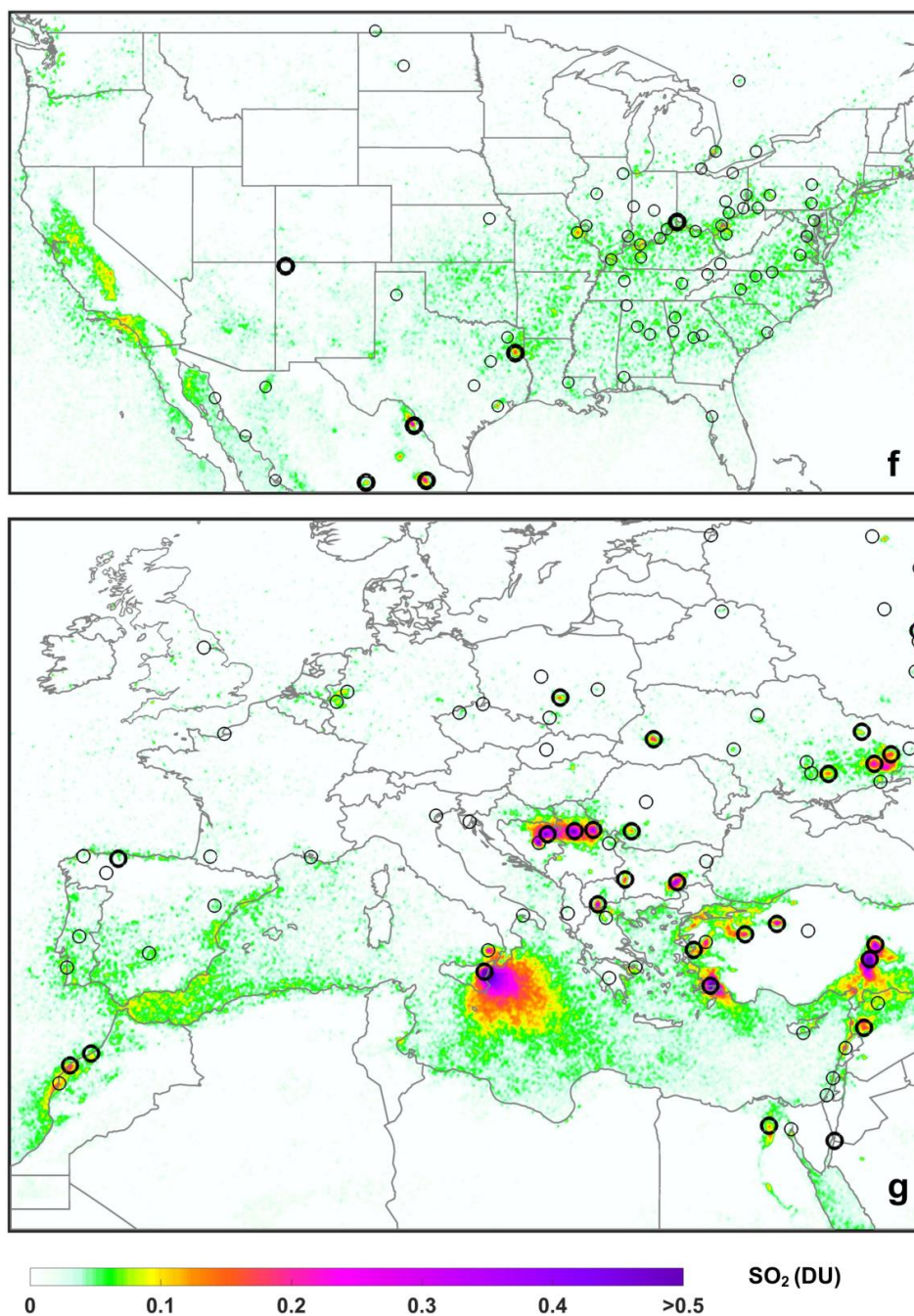
1  
2 Figure 6. Continued.





1  
2

3 Figure 6. Continued. The gray lines are the topography isolines (in meter). Note that to further  
4 reduce the data scatter, the SO<sub>2</sub> map was smoothed by a 2-dimensional 20-points box car function  
5 (instead of 10-points function for the other sub-figures).



1  
2  
3

Figure 6. Continued.



## 1 5. EMISSIONS ESTIMATES

2

3 Satellite observations are being increasingly used to estimate SO<sub>2</sub> emissions. In particular, new  
4 methods have been very successful in deriving reliable emission rates, and even detecting missing  
5 sources, by combining satellite SO<sub>2</sub> columns and wind information, without the need of  
6 atmospheric chemistry transport models (e.g., Beirle et al., 2014; Fioletov et al., 2016, 2017, 2020;  
7 McLinden et al., 2016; Carn et al., 2017). These techniques have been used to derive global SO<sub>2</sub>  
8 emissions inventory from OMI observations (Liu et al., 2018). Recently, Fioletov et al. (2020)  
9 presented an analysis using the TROPOMI operational SO<sub>2</sub> product and found overall consistent  
10 results with the OMI emissions estimates. The TROPOMI-based emissions uncertainties were  
11 found a factor of 1.5 - 2 lower than the ones from OMI. In this section, we repeat the same analysis  
12 using the COBRA SO<sub>2</sub> retrievals and investigate the added value of COBRA for the estimation of  
13 SO<sub>2</sub> emissions. The details of the inversion technique can be found in Fioletov et al. (2015) and  
14 references above.

15 In brief, the method considers a potential point source and apply a wind rotation of the satellite  
16 measured SO<sub>2</sub> VCDs around this location. This first step enables to align all plume dispersion  
17 patterns along a fixed direction and leads to an improved SO<sub>2</sub> detection limit. By contrasting the  
18 upwind and downwind averaged SO<sub>2</sub> columns, the wind rotation procedure allows to confirm  
19 whether the test location is a real emission source and also to correct for a possible bias in the data.  
20 Note that for this first step, the retrieved SO<sub>2</sub> VCDs are rescaled using site-specific AMFs so that  
21 realistic SO<sub>2</sub> emission profile shapes (based on the elevation of the site and climatological  
22 boundary-layer height) are used for all analyzed sources.

23 The second part of the retrieval method deals with the emission estimate itself. The averaged  
24 downwind SO<sub>2</sub> field is modelled by an exponential modified Gaussian function which accounts  
25 for the SO<sub>2</sub> total mass, e-folding time and plume width. From the fitted parameters, the average  
26 SO<sub>2</sub> emission rate can be derived directly. Here the baseline inversion is however not to fit all three  
27 parameters but rather to prescribe the e-folding time and plume width, and therefore the only  
28 parameter derived from the fit is the SO<sub>2</sub> total mass which is directly proportional to the SO<sub>2</sub>  
29 emission rate.

30

31

32

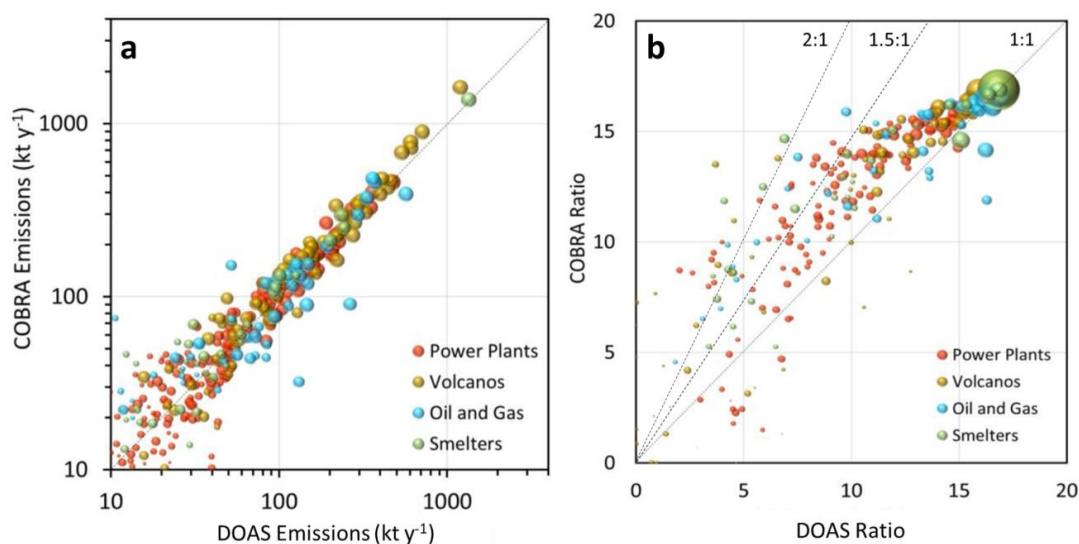


1

## 2 5.1 SO<sub>2</sub> emissions for large sources

3 The method was applied to the SO<sub>2</sub> data from COBRA for 274 large emissions sources, including  
4 power plants, volcanoes, oil and gas sources and smelters, distributed worldwide. In Fig. 7a, the  
5 results are compared to the analysis of Fioletov et al. (2020) using the TROPOMI DOAS product,  
6 for the period from April 2018 to March 2019.

7



8

9 Figure 7. (a) Estimated SO<sub>2</sub> emissions from TROPOMI, based on the COBRA and DOAS  
10 algorithms analyzed for power plants, volcanoes, oil and gas industries, smelters sources. (b)  
11 Ratios of the estimated emissions and the corresponding uncertainties. The size of the marker is  
12 proportional to the estimated SO<sub>2</sub> emission.

13

14 In general, the emission estimates from COBRA and DOAS are fairly consistent for all four source  
15 types. However, it was found that the local bias in the satellite data (as derived from the upwind  
16 SO<sub>2</sub> columns) are much lower with COBRA (~0.05 DU) than with DOAS (~0.25 DU), consistent  
17 with previous findings (Section 3). Also, as result of the large improvement in the noise level, the  
18 estimated emissions uncertainties are significantly improved with COBRA compared to DOAS,  
19 by 20-50% on average (see Fig. 7b).

20 It should be emphasized though that the improvement of emission uncertainties depends on the  
21 emission level. The sources considered here are relatively large sources that have been previously



1 detected by OMI. The TROPOMI COBRA SO<sub>2</sub> data set presented in this study combines the  
2 advantages of high spatial resolution, low noise level and almost no bias. It has therefore the  
3 potential to detect weaker sources (as shown in Sect. 4).

#### 4 **5.2. Detection of weak emissions**

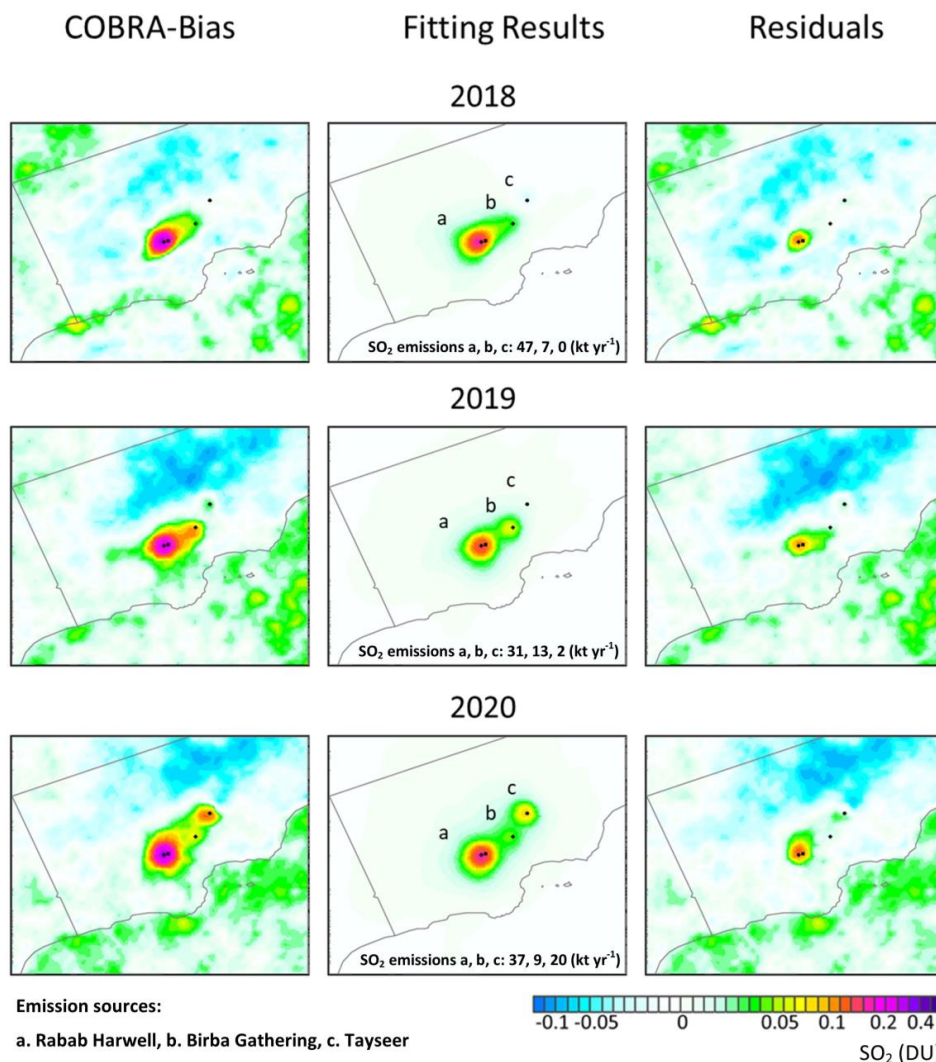
5 It is enlightening to estimate the lowest level of SO<sub>2</sub> emission detectable by COBRA. Clearly, it  
6 is expected to be dependent on the observation conditions and generally speaking the best detection  
7 limit is obtained for sites with low noise on the SO<sub>2</sub> SCDs and the highest measurement sensitivity  
8 (i.e. high AMFs). These sites are found at low latitudes and in particular at high elevations or for  
9 high albedos. To estimate the emission detection limit, we define the statistical significance of an  
10 emission signal as three times its standard error. Based on the global sources presented above  
11 (section 5.1), we performed statistics using this metric. To avoid biases by the strongest sources,  
12 we only considered the sources with estimated emissions less than 50 kt y<sup>-1</sup>. The resulting detection  
13 limit values are found in the range between 4 and 11 kt y<sup>-1</sup> depending on the AMF, with a mean  
14 value of 8 kt y<sup>-1</sup>. It is important to realize that this limit of detection is remarkably low, at least  
15 twice better than using TROPOMI DOAS data. It is also a factor of 4 smaller than the detection  
16 limit of 30-40 kt y<sup>-1</sup> offered by OMI for the first years of operation (Fioletov et al., 2016; McLinden  
17 et al., 2016). This suggests that the TROPOMI COBRA implementation is optimal in exploiting  
18 the gain in spatial resolution of TROPOMI compared to OMI (~16 times smaller pixel sizes). This  
19 finding is actually supported by the fact that the noise levels for individual pixels for TROPOMI  
20 COBRA and OMI PCA VCDs are similar (not shown; see also section 3 of Fioletov et al., 2020).

21 In the following, we demonstrate the potential of the TROPOMI COBRA SO<sub>2</sub> data set to detect  
22 and quantify weak emissions. For this, we use a slightly adapted version of the inversion technique  
23 of section 5.1, and illustrate the method on a selection of new emission sources.

24 The region of interest is the Dhofar governorate in southern Oman. There, the exploitation of oil  
25 and gas fields is growing fast, with a number of rapidly evolving projects of exploration and  
26 production. In Figure 8 (left column), the yearly averaged TROPOMI SO<sub>2</sub> maps over South Oman  
27 are shown for 2018-2020. One can clearly identify and isolate 3 main emission locations, namely  
28 the Rabab Harwell integrated plant (18.03°N, 54.64°E), the Birba Gathering station (18.32°N,  
29 55.10°E) and the Tayseer gas field (18.71°N, 55.34°E). We note that these emission sources are



1 not listed in any emission inventory and the actual locations of the sources are approximated from  
2 available visible imagery (e.g. Google Earth). A noticeable feature in Figure 8 is the very low  
3 observed SO<sub>2</sub> column level, in particular over Birba Gathering and Tayseer with SO<sub>2</sub> VCDs of 0.03  
4 – 0.1 DU, reflecting again the great sensitivity of COBRA. To estimate the SO<sub>2</sub> emissions from  
5 the TROPOMI data, the source method used in section 5.1 has been refined and tuned for this  
6 particular case study. A multi-source SO<sub>2</sub> emission retrieval was applied as in Fioletov et al. (2017)  
7 with one modification: a regression term proportional to the elevation was added to the fit to adjust  
8 for a small altitude-related bias in retrieved SO<sub>2</sub> (the values were slightly lower over the mountains  
9 near the Arabian Sea coast). This multi-source method is motivated by the fact that the sources are  
10 close to each other (~ 50-100 km distance) and the emissions cannot be fitted separately. Here, the  
11 approach basically allows for overlaps of the modelled SO<sub>2</sub> spatial distributions; the emissions  
12 from the individual sources are then adjusted so that the total SO<sub>2</sub> modelled field fits best the  
13 observed SO<sub>2</sub> VCD distribution. In Figure 8, the results of the fit are shown (center column), as  
14 well as the residuals of the fit (right column). The estimated annual SO<sub>2</sub> emissions for the 3 sources  
15 are given in the inset of Figure 8. Note that for this particular case, the emission detection limit (as  
16 defined above) is typically of about 6 kt yr<sup>-1</sup>. For the Rabab Harwell site, the algorithm retrieves  
17 rather high and stable emissions over the years, with an average value of about 40 kt yr<sup>-1</sup>, which is  
18 well above the estimated detection limit. Interestingly, the Rabab Harwell site has large residuals  
19 of ~0.1 DU for all years. This suggests that the point source representation used here is likely not  
20 sufficient to explain the observations and it is possible that there are many small contributing  
21 sources in the area. For the Birba Gathering site, the estimated emissions are much smaller and lie  
22 in the range of 7-13 kt yr<sup>-1</sup>. Yet, there is a good confidence that these emissions are real, given that  
23 the estimates are a factor of 1-2 larger than the limit of detection. However, it is clear that the  
24 uncertainty of the emission estimates are quite large. For the Tayseer site, an SO<sub>2</sub> signal could be  
25 detected only recently. In 2019, the estimated emissions are of 2 kt yr<sup>-1</sup>, i.e. below the detection  
26 limit, and in 2020, the SO<sub>2</sub> emissions strongly increased to about 20 kt yr<sup>-1</sup>, probably as a result of  
27 a change in operation at the production facility. Finally, note that no significant residuals could be  
28 found neither for Tayseer nor Birba Gathering site, and this suggests a point source behavior, at  
29 both sites.



1

2 Figure 8. (Left) Yearly mean TROPOMI SO<sub>2</sub> columns retrieved from COBRA over South Oman  
3 for 2018 (April to December), 2019, 2020 (from top to bottom), after bias correction for the effect  
4 of elevation (see text). Three distinct SO<sub>2</sub> spots are discernable from the maps and are the results  
5 of emissions from oil and gas fields, referred as Rabab Harwell, Birba Gathering and Tayseer,  
6 (center) results of the fitting of TROPOMI SO<sub>2</sub> data. The estimated annual SO<sub>2</sub> emissions (given  
7 in the inset for the three sources) are used to reconstruct the SO<sub>2</sub> column field, (right) residuals of  
8 the fit or the difference between TROPOMI and fitting results.



1 In summary, the analysis over South Oman of Figure 8 nicely illustrates the strength of a highly  
2 sensitive scheme such as COBRA when applied to a high spatial resolution instrument as  
3 TROPOMI. The fact that such low SO<sub>2</sub> emissions can be tracked and quantified with that level of  
4 detail is remarkable. Although not shown, the emission inversion scheme was successfully applied  
5 not only to the South Oman sources but also to other test sites, as they were found in the global  
6 SO<sub>2</sub> map (Figure 6). The wind-rotation technique when applied to TROPOMI COBRA SO<sub>2</sub> data  
7 is arguably a promising tool to monitor weak SO<sub>2</sub> emissions and track the activity from rapidly  
8 emerging production facilities worldwide. However, applying the inversion scheme at the global  
9 scale is a significant effort, as it also requires some level of manual intervention and testing. For  
10 instance, the information on source type, location, etc. is typically lacking, and the supporting  
11 visible imagery - useful for identifying industrial facilities - is often outdated.

## 12 **6. CONCLUSIONS**

13

14 A new spectral fitting method for the retrieval of sulfur dioxide columns in the UV was presented  
15 and demonstrated for TROPOMI. Based on a dynamical total measurement error covariance, the  
16 method, called COBRA, allows reducing considerably the noise level (by a factor of 2) and biases  
17 present in the current TROPOMI DOAS SO<sub>2</sub> operational product. COBRA provides greater  
18 sensitivity to low SO<sub>2</sub> columns, and this conclusion is supported by MAX-DOAS observations.  
19 Preliminary comparison of COBRA to PCA retrievals suggests similar and even better algorithm  
20 performance. The SO<sub>2</sub> vertical column precision for individual pixel is in the range 0.5 - 1 DU;  
21 the systematic VCD uncertainty (contribution from the COBRA spectral fit only) is very small,  
22 typically less than 0.04 DU.

23 The benefit of COBRA is clearly demonstrated in this work using long-term oversampled  
24 averages. Owing to the excellent quality of the data (in terms of precision and accuracy), the high  
25 spatial resolution of TROPOMI can be better exploited. Zoomed SO<sub>2</sub> maps reveal new emission  
26 sources worldwide, with low SO<sub>2</sub> columns of 0.05 - 0.2 DU, or even lower.

27 By using the COBRA SO<sub>2</sub> data over large emission sources, we have recalculated the SO<sub>2</sub>  
28 emissions obtained by Fioletov et al. (2020) that were based on the TROPOMI operational SO<sub>2</sub>  
29 product. While the derived emission rates agree generally well, we found that the uncertainties on  
30 the emissions are significantly lower (up to 50%) using COBRA than with the operational product.





1 This opens the possibility to retrieve SO<sub>2</sub> emissions for weakly emitting sources, and we present a  
2 number of examples that demonstrate the potential of the COBRA data in this direction.

3 With an estimated annual emission detection limit of about 8 kt yr<sup>-1</sup>, the TROPOMI COBRA SO<sub>2</sub>  
4 data provides unique access to weak anthropogenic and volcanic point sources, and can help  
5 completing current SO<sub>2</sub> emission inventories. It can also be used to track more accurately weak or  
6 rapid changes in SO<sub>2</sub> levels, e.g., due to COVID-19 lockdown measures (Levelt et al., 2021) as  
7 well as estimate seasonal and even monthly emissions. Finally, COBRA data would be particularly  
8 relevant for the CAMS assimilation system as well.

9 COBRA is a good candidate for an implementation in the TROPOMI operational processor, with  
10 limited computational resources and without the need for a separate background correction processor.  
11 COBRA is also adaptable to other satellite instruments, including from geostationary platforms.  
12 In particular, the European Sentinel-4 mission would likely benefit from a COBRA approach for  
13 the retrieval of SO<sub>2</sub> columns, as the atmosphere will be sounded under unfavorable large  
14 observation angles.

15 Future work could also be dedicated to the application of COBRA to historical sensors, in order to  
16 produce a consistent long-term SO<sub>2</sub> data record, but also to the retrieval of other molecules.

17

18

19

20

21

22

23

24

25



## 1 **CODE AND DATA AVAILABILITY**

2 The TROPOMI COBRA SO<sub>2</sub> dataset is available from the corresponding author on request. The  
3 TROPOMI DOAS SO<sub>2</sub> product is publically available on the Copernicus Sentinel-5P data hub  
4 (<https://s5phub.copernicus.eu>). The TROPOMI PCA SO<sub>2</sub> dataset is available from Dr. Can Li on  
5 request. The OMPS PCA SO<sub>2</sub> is publically available from Goddard Earth Sciences (GES) Data  
6 Information Service Center (DISC)  
7 ([https://daac.gsfc.nasa.gov/datasets/OMPS\\_NPP\\_NMSO2\\_PCA\\_L2\\_2/summary](https://daac.gsfc.nasa.gov/datasets/OMPS_NPP_NMSO2_PCA_L2_2/summary)).  
8 The CAMS regional data are available from the Copernicus Atmosphere Data Store  
9 (<https://atmosphere.copernicus.eu/data/>). The SO<sub>2</sub> emissions estimates can be obtained from Dr.  
10 Vitali Fioletov on request. The MAX-DOAS measurements used to validate the satellite SO<sub>2</sub> data  
11 are available on request from Drs. François Hendrick (Xianghe), Thomas Wagner, Vinod Kumar  
12 (Mohali).

## 13 **AUTHOR CONTRIBUTIONS**

14 N.T. prepared the manuscript and figures with contributions from all the coauthors. N.T., I.D.S.,  
15 C.Le., L.C., J.V., H.B., M.V.R. contributed to the development of the COBRA algorithm,  
16 processing of the data and satellite comparison. V.F., C.McL., D.G. estimated the SO<sub>2</sub> emissions.  
17 C.Li, N.K. developed the TROPOMI and OMPS PCA algorithms and provided data for the  
18 comparison. P.H. and D.L. contributed to the development of the TROPOMI DOAS algorithm,  
19 processing of the data and satellite comparison. A.I. and R.R. provided CAMS SO<sub>2</sub> data. T. W.,  
20 V.K., F.H, M.V.R. analyzed and provided MAX-DOAS data. All authors contributed to the  
21 interpretation of the results and improvement of the manuscript.

## 22 **COMPETING INTERESTS,**

23 The authors declare that they have no conflict of interest.

## 24 **ACKNOWLEDGEMENTS AND FINANCIAL SUPPORT**

25 We acknowledge financial support from ESA S5P MPC (4000117151/16/I-LG), Belgium Prodex  
26 TRACE-S5P (PEA 4000105598) and TROVA (PEA 4000130630) projects. We thank  
27 EU/ESA/KNMI/DLR for providing the TROPOMI/S5P Level 1 products. This paper contains modified  
28 Copernicus data (2018/2020) processed by BIRA-IASB.



1 C.Li and N.K. acknowledge support from the NASA Earth Science Division Aura Science Team,  
2 Suomi NPP Science Team and US participating investigator programs. L. C. is a research associate  
3 supported by the Belgian F.R.S-FNRS. We acknowledge Pucai Wang and Ting Wang (IAP/CAS,  
4 China) for their support in operating and maintaining MAX-DOAS observations in Xianghe. We  
5 acknowledge Dr. Vinayak Sinha for supporting us with the logistics to operate the MAX-DOAS  
6 at Mohali. V.K. acknowledges the Alexander von Humboldt foundation for supporting the  
7 postdoctoral fellowship.

8

## 9 REFERENCES

- 10 Afe, O. T., Richter, A., Sierk, B., Wittrock, F., and Burrows, J.P.: BrO emissions from volcanoes:  
11 a survey using GOME and SCIAMACHY measurements, *Geophys. Res. Lett.*, 31, L24113, 2004.
- 12
- 13 Beirle, S., Hörmann, C., Penning de Vries, M., Dörner, S., Kern, C., and Wagner, T.: Estimating  
14 the volcanic emission rate and atmospheric lifetime of SO<sub>2</sub> from space: a case study for Kīlauea  
15 volcano, Hawai'i, *Atmos. Chem. Phys.*, 14, 8309–8322, [https://doi.org/10.5194/acp-14-8309-](https://doi.org/10.5194/acp-14-8309-2014)  
16 2014, 2014.
- 17 Bogumil, K., Orphal, J., Homann, T., Voigt, S., Spietz, P., Fleischmann, O., Vogel, A., Hartmann,  
18 M., Bovensmann, H., Frerick, J., and Burrows, J. P.: Measurements of molecular absorption  
19 spectra with the SCIAMACHY Pre-Flight Model: instrument characterization and reference data  
20 for atmospheric remote-sensing in the 230–2380nm region, *J. Photoch. Photobiol. A*, 157, 167–  
21 184, 2003.
- 22 Carn, S.A., Fioletov, V.E., McLinden, C.A., Li, C., and Krotkov, N.A.: A decade of global  
23 volcanic SO<sub>2</sub> emissions measured from space, *Sci. Rep.*, 7, 44095; doi:10.1038/srep44095, 2017.
- 24
- 25 Clarisse, L., Clerbaux, C., Franco, B., Hadji-Lazaro, J., Whitburn, S., Kopp, A. K., et al.: A decadal  
26 data set of global atmospheric dust retrieved from IASI satellite measurements. *J. Geophys. Res.*  
27 *Atmos.*, 124, <https://doi.org/10.1029/2018JD029701>, 2019



- 1 Clarisse, L., Van Damme, M., Clerbaux, C., and Coheur, P.-F.: Tracking down global NH<sub>3</sub> point  
2 sources with wind-adjusted superresolution, *Atmos. Meas. Tech.*, 12, 5457–5473,  
3 <https://doi.org/10.5194/amt-12-5457-2019>, 2019.
- 4 Compernelle, S., Argyrouli, A., Lutz, R., Sneep, M., Lambert, J.-C., Fjæraa, A. M., Hubert, D.,  
5 Keppens, A., Loyola, D., O'Connor, E., Romahn, F., Stammes, P., Verhoelst, T., and Wang, P.:  
6 Validation of the Sentinel-5 Precursor TROPOMI cloud data with Cloudnet, Aura OMI O<sub>2</sub>-O<sub>2</sub>,  
7 MODIS and Suomi-NPP VIIRS, *Atmos. Meas. Tech. Discuss.*, [https://doi.org/10.5194/amt-2020-](https://doi.org/10.5194/amt-2020-122)  
8 122, in review, 2020.
- 9 Danckaert, T., Fayt, C., Van Roozendael, M., De Smedt, I., Letocart, V., Merlaud, A., Pinardi, G:  
10 Qdoas Software User Manual, Version 3.2, [http://uv-](http://uv-vis.aeronomie.be/software/QDOAS/QDOAS_manual.pdf)  
11 [vis.aeronomie.be/software/QDOAS/QDOAS\\_](http://uv-vis.aeronomie.be/software/QDOAS/QDOAS_manual.pdf) manual.pdf (last access: 24 April 2020), 2017.
- 12
- 13 Eisinger, M., and Burrows, J.P.: Tropospheric sulfur dioxide observed by the ERS-2 GOME  
14 instrument, *Geophys. Res. Lett.*, Vol. 25, pp. 4177-4180, 1998.
- 15 Eskes, H. J., and Boersma, K. F.: Averaging kernels for DOAS total column satellite retrievals,  
16 *Atmos. Chem. Phys.*, 3, 1285–1291, 2003.
- 17 Franco, B., Clarisse, L., Stavrou, T., Müller, J.-F., Van Damme, M., Whitburn, S., Hadji-Lazaro,  
18 J., Hurtmans, D., Taraborrelli, D., Clerbaux, C., and Coheur, P.-F.: A General Framework for  
19 Global Retrievals of Trace Gases From IASI: Application to Methanol, Formic Acid, and PAN, *J.*  
20 *Geophys. Res. Atmos.*, Volume 123, Pages 13,963-13,984, 2018.
- 21
- 22 Fioletov, V. E., McLinden, C. A., Krotkov, N., Yang, K., Loyola, D. G., Valks, P.,  
23 Theys, N., Van Roozendael, M., Nowlan, C. R., Chance, K., Liu, X., Lee, C.,  
24 and Martin, R. V.: Application of OMI, SCIAMACHY, and GOME-2 satellite SO<sub>2</sub> retrievals for  
25 detection of large emission sources, *J. Geophys. Res. Atmos.*, 118, 11,399–11,418,  
26 [doi:10.1002/jgrd.50826](https://doi.org/10.1002/jgrd.50826), 2013.
- 27



- 1 Fioletov, V. E., McLinden, C. A., Krotkov, N. A., and Li, C.: Lifetimes and emissions of SO<sub>2</sub>  
2 from point sources estimated from OMI, *Geophys. Res. Lett.*, 42, 1–8,  
3 <https://doi.org/10.1002/2015GL063148>, 2015.
- 4
- 5 Fioletov, V. E., McLinden, C. A., Krotkov, N., Li, C., Joiner, J., Theys, N., Carn, S. and Moran,  
6 M. D.: A global catalogue of large SO<sub>2</sub> sources and emissions derived from the Ozone Monitoring  
7 Instrument, *Atmos. Chem. Phys.*, 16(18), 11497–11519, doi:10.5194/acp-16-11497-2016, 2016.
- 8
- 9 Fioletov, V., McLinden, C. A., Kharol, S. K., Krotkov, N. A., Li, C., Joiner, J., Moran, M. D., Vet,  
10 R., Visschedijk, A. J. H., and Denier van der Gon, H. A. C.: Multi-source SO<sub>2</sub> emission retrievals  
11 and consistency of satellite and surface measurements with reported emissions, *Atmos. Chem.*  
12 *Phys.*, 17, 12597–12616, <https://doi.org/10.5194/acp-17-12597-2017>, 2017.
- 13
- 14 Fioletov, V., McLinden, C.A., Griffin, D., Theys, N., Loyola, D.G., Hedelt, P., Krotkov, N.A., Li,  
15 C.: Anthropogenic and volcanic point source SO<sub>2</sub> emissions derived from TROPOMI onboard  
16 Sentinel 5 Precursor: first results, *Atmos. Chem. Phys.*, 20, 5591–5607,  
17 <https://doi.org/10.5194/acp-20-5591-2020>, 2020.
- 18
- 19 Hönninger, G. and Platt, U.: Observations of BrO and its vertical distribution during surface ozone  
20 depletion at Alert, *Atmos. Environ.*, 36, 2481–2489, 2002.
- 21
- 22 Hörmann, C., Sihler, H., Bobrowski, N., Beirle, S., Penning de Vries, M., Platt, U., and  
23 Wagner, T.: Systematic investigation of bromine monoxide in volcanic plumes from space by  
24 using the GOME-2 instrument, *Atmos. Chem. Phys.*, 13, 4749–4781, doi:10.5194/acp-13-4749-  
25 2013, 2013.
- 26
- 27 Inness, A., Ades, M., Agustí-Panareda, A., Barré, J., Benedictow, A., Blechschmidt, A.-M.,  
28 Dominguez, J. J., Engelen, R., Eskes, H., Flemming, J., Huijnen, V., Jones, L., Kipling, Z.,  
29 Massart, S., Parrington, M., Peuch, V.-H., Razinger, M., Remy, S., Schulz, M., and Suttie, M.: The  
30 CAMS reanalysis of atmospheric composition, *Atmos. Chem. Phys.*, 19, 3515–3556,  
31 <https://doi.org/10.5194/acp-19-3515-2019>, 2019.



1

2 Khokhar, M. F., Frankenberg, C., Van Roozendaal, M., Beirle, S., Kühl, S., Richter, A., Platt, U.,  
3 and Wagner, T.: Satellite Observations of Atmospheric SO<sub>2</sub> from Volcanic Eruptions during the  
4 Time Period of 1996 to 2002, *J. Adv. Space Res.*, 36(5), 879-887, 10.1016/j.asr.2005.04.114, 2005.

5 Krotkov, N. A., Carn, S. A., Krueger, A. J., Bhartia, P. K., Yang, K.: Band residual difference  
6 algorithm for retrieval of SO<sub>2</sub> from the Aura Ozone Monitoring Instrument (OMI), *IEEE Trans.*  
7 *Geosci. Remote Sensing*, AURA Special Issue, 44(5), 1259-1266,  
8 doi:10.1109/TGRS.2005.861932, 2006.

9 Krotkov, N. A., McLinden, C. A., Li, C., Lamsal, L. N., Celarier, E. A., Marchenko, S. V., Swartz,  
10 W. H., Bucseła, E. J., Joiner, J., Duncan, B. N., Boersma, K. F., Veeffkind, J. P., Levelt, P. F.,  
11 Fioletov, V. E., Dickerson, R. R., He, H., Lu, Z., and Streets, D. G.: Aura OMI observations of  
12 regional SO<sub>2</sub> and NO<sub>2</sub> pollution changes from 2005 to 2015, *Atmos. Chem. Phys.*, 16(7), 4605-  
13 4629. DOI: 10.5194/acp-15-4605-2016, 2016.

14

15 Krueger, A. J.: Sighting of El Chichon sulfur dioxide clouds with the Nimbus 7 total ozone  
16 mapping spectrometer, *Science*, 220, 1377–1379, 1983.

17

18 Kumar, V., Beirle, S., Dörner, S., Mishra, A. K., Donner, S., Wang, Y., Sinha, V., and Wagner,  
19 T.: Long-term MAX-DOAS measurements of NO<sub>2</sub>, HCHO, and aerosols and evaluation of  
20 corresponding satellite data products over Mohali in the Indo-Gangetic Plain, *Atmos. Chem. Phys.*,  
21 20, 14183–14235, <https://doi.org/10.5194/acp-20-14183-2020>, 2020.

22 Levelt, P. F., et al., Air Quality Impacts of COVID-19 Lockdown Measures detected from space  
23 using high spatial resolution observations of multiple trace gases of Sentinel-5P/TROPOMI, in  
24 preparation for *Atmos. Chem. Phys. Discuss.*, 2021.

25

26 Li, C., Joiner, J., Krotkov, N. A. and Bhartia, P. K.: A fast and sensitive new satellite SO<sub>2</sub> retrieval  
27 algorithm based on principal component analysis: Application to the ozone monitoring instrument,  
28 *Geophys. Res. Lett.*, 40(23), 6314–6318, doi:10.1002/2013GL058134, 2013.

29



- 1 Li, C., Krotkov, N. A., Leonard, P. J. T., Carn, S., Joiner, J., Spurr, R. J. D., and Vasilkov, A.:  
2 Version 2 Ozone Monitoring Instrument SO<sub>2</sub> product (OMSO2 V2): new anthropogenic  
3 SO<sub>2</sub> vertical column density dataset, *Atmos. Meas. Tech.*, 13, 6175–6191,  
4 <https://doi.org/10.5194/amt-13-6175-2020>, 2020a.  
5
- 6 Li, C., Krotkov, N. A., Leonard, P., and Joiner, J.: OMI/Aura Sulphur Dioxide (SO<sub>2</sub>) Total Column  
7 1-orbit L2 Swath 13x24 km V003, Greenbelt, MD, USA, Goddard Earth Sciences Data and  
8 Information Services Center (GES DISC), Accessed: June 2020, 10.5067/Aura/OMI/DATA2022,  
9 2020b.  
10
- 11 Li, C., Krotkov, N. A., Leonard, P., and Joiner, J.: OMPS/NPP PCA SO<sub>2</sub> Total Column 1-Orbit  
12 L2 Swath 50x50km V2, Greenbelt, MD, USA, Goddard Earth Sciences Data and Information  
13 Services Center (GES DISC), Accessed: June 2020, 10.5067/MEASURES/SO2/DATA205,  
14 2020c.  
15
- 16 Liu, F., Choi, S., Li, C., Fioletov, V. E., McLinden, C. A., Joiner, J., Krotkov, N. A., Bian, H.,  
17 Janssens-Maenhout, G., Darmenov, A. S., and da Silva, A. M.: A new global anthropogenic SO<sub>2</sub>  
18 emission inventory for the last decade: A mosaic of satellite-derived and bottom-up emissions,  
19 *Atmos. Chem. Phys.* 18, 16571-16586, <https://doi.org/10.5194/acp-18-16571-2018> , 2018.  
20
- 21 Loyola, D. G., Gimeno García, S., Lutz, R., Argyrouli, A., Romahn, F., Spurr, R. J. D., Pedernana,  
22 M., Doicu, A., Molina García, V., and Schüssler, O.: The operational cloud retrieval algorithms  
23 from TROPOMI on board Sentinel-5 Precursor, *Atmos. Meas. Tech.*, 11, 409–427,  
24 <https://doi.org/10.5194/amt-11-409-2018>, 2018.  
25
- 26 McLinden, C. A., Fioletov, V., Shephard, M. W., Krotkov, N., Li, C., Martin, R. V., Moran, M.  
27 D. and Joiner, J.: Space-based detection of missing sulfur dioxide sources of global air pollution,  
28 *Nat. Geosci.*, 9(7), 496–500, doi:10.1038/ngeo2724, 2016.  
29
- 30 Nowlan, C.R., Liu, X., Chance, K., Cai, Z., Kurosu, T.P., Lee, C., and Martin, R.V.: Retrievals of  
31 sulfur dioxide from the Global Ozone Monitoring Experiment 2 (GOME-2) using an optimal



- 1 estimation approach: Algorithm and initial validation, *J. Geophys. Res.*, 116, D18301,  
2 doi:10.1029/2011JD015808, 2011.
- 3
- 4 Platt, U., and Stutz, J.: Differential Optical Absorption Spectroscopy (DOAS), Principle and  
5 Applications, ISBN 3-340-21193-4, Springer Verlag, Heidelberg, 2008.
- 6 Queißer, M., Burton, M., Theys, N., Pardini, F., Salerno, G., Caltabiano, T., Varnham, M., Esse,  
7 B., and Kazahaya, R.: TROPOMI enables high resolution SO<sub>2</sub> flux observations from Mt. Etna  
8 (Italy), and beyond, *Nature Scientific Reports*, volume 9, Article number: 957,  
9 <https://doi.org/10.1038/s41598-018-37807-w>, 2019.
- 10
- 11 Rix, M., Valks, P., Hao, N., Loyola, D. G., Schlager, H., Huntrieser, H. H., Flemming, J., Koehler,  
12 U., Schumann, U., and Inness, A.: Volcanic SO<sub>2</sub>, BrO and plume height estimations using GOME-  
13 2 satellite measurements during the eruption of Eyjafjallajökull in May 2010, *J. Geophys. Res.*,  
14 117, D00U19, doi:10.1029/2011JD016718, 2012.
- 15
- 16 Rodgers, C. D.: *Inverse Methods for Atmospheric Sounding, Theory and Practice*, World  
17 Scientific Publishing, Singapore-New-Jersey-London-Hong Kong, 2000.
- 18
- 19 Theys, N., De Smedt, I., van Gent, J., Danckaert, T., Wang, T., Hendrick, F., Stavrakou, T.,  
20 Bauduin, S., Clarisse, L., Li, C., Krotkov, N. A., Yu, H., Van Roozendael, M.: Sulfur dioxide  
21 vertical column DOAS retrievals from the Ozone Monitoring Instrument: Global observations and  
22 comparison to ground-based and satellite data, *J. Geophys. Res. Atmos.*, 120,  
23 doi:10.1002/2014JD022657, 2015.
- 24
- 25 Theys, N., De Smedt, I., Yu, H., Danckaert, T., van Gent, J., Hörmann, C., Wagner, T., Hedelt, P.,  
26 Bauer, H., Romahn, F., Pedergnana, M., Loyola, D. and Van Roozendael, M.: Sulfur dioxide  
27 retrievals from TROPOMI onboard Sentinel-5 Precursor: algorithm theoretical basis, *Atmos.*  
28 *Meas. Tech.*, 10(1), 119–153, doi:10.5194/amt-10-119-2017, 2017.





1

2 Theys, N., Hedelt, P., Smedt, I. De, Lerot, C., Yu, H., Vlietinck, J., Pedernana, M., Arellano, S.,  
3 Galle, B., Fernandez, D., Barrington, C., Taine, B., Loyola, D., Van Roozendael, M.: Global  
4 monitoring of volcanic SO<sub>2</sub> degassing from space with unprecedented resolution, *Nature Scientific*  
5 Reports, volume 9, Article number: 2643, <https://doi.org/10.1038/s41598-019-39279-y>, 2019.

6

7 Tirpitz, J.-L., Frieß, U., Hendrick, F., Alberti, C., Allaart, M., et al.: Intercomparison of MAX-  
8 DOAS vertical profile retrieval algorithms: studies on field data from the CINDI-2 campaign,  
9 *Atmos. Meas. Tech.*, 14, 1–35, <https://doi.org/10.5194/amt-14-1-2021>, 2021.

10

11 Van Damme, M., Clarisse, L., Heald, C. L., Hurtmans, D., Ngadi, Y., Clerbaux, C., Dolman, A.  
12 J., Erisman, J.W., and Coheur, P. F.: Global distributions, time series and error characterization of  
13 atmospheric ammonia (NH<sub>3</sub>) from IASI satellite observations, *Atmos. Chem. Phys.*, 14, 2905–  
14 2922, <https://doi.org/10.5194/acp-14-2905-2014>, 2014.

15 Veefkind, J. P., Aben, I., McMullan, K., Förster, H., de Vries, J., Otter, G., Claas, J., Eskes, H. J.,  
16 de Haan, J. F., Kleipool, Q., van Weele, M., Hasekamp, O., Hoogeveen, R., Landgraf, J., Snel, R.,  
17 Tol, P., Ingmann, P., Voors, R., Kruizinga, B., Vink, R., Visser, H., and Levelt, P. F.: TROPOMI  
18 on the ESA Sentinel-5 Precursor: A GMES mission for global observations of the atmospheric  
19 composition for climate, air quality and ozone layer applications, *Remote Sens. Environ.*, 120, 70–  
20 83, [doi:10.1016/j.rse.2011.09.027](https://doi.org/10.1016/j.rse.2011.09.027), 2012.

21 von Clarmann, T., Grabowski, U., and Kiefer, M.: On the role of non-random errors in inverse  
22 problems in radiative transfer and other applications, *J. Quant. Spectros. Ra.*, 71, 39–46, 2001.

23 Walker, J. C., Dudhia, A., and Carboni, E.: An effective method for the detection of trace species  
24 demonstrated using the MetOp Infrared Atmospheric Sounding Interferometer, *Atmos. Meas.*  
25 *Tech.*, 4, 1567–1580, <https://doi.org/10.5194/amt-4-1567-2011>, 2011.

26 Wang, T., Hendrick, F., Wang, P., Tang, G., Clémer, K., Yu, H., Fayt, C., Hermans, C.,  
27 Gielen, C., Müller, J.-F., Pinaridi, G., Theys, N., Brenot, H., and Van Roozendael, M.: Evaluation  
28 of tropospheric SO<sub>2</sub> retrieved from MAX-DOAS measurements in Xianghe, China, *Atmos. Chem.*  
29 *Phys.*, 14, 11149–11164, [doi:10.5194/acp-14-11149-2014](https://doi.org/10.5194/acp-14-11149-2014), 2014.



1

2 Yang, K., Krotkov, N., Krueger, A., Carn, S., Bhartia, P. K., and Levelt, P.: Retrieval of Large  
3 Volcanic SO<sub>2</sub> columns from the Aura Ozone Monitoring Instrument (OMI): Comparisons and  
4 Limitations, *J. Geophys. Res.*, 112, D24S43, doi:10.1029/2007JD008825, 2007.

5

6 Yang, K., Liu, X., Bhartia, P., Krotkov, N., Carn, S., Hughes, E., Krueger, A., Spurr, R., Trahan,  
7 S.: Direct retrieval of sulfur dioxide amount and altitude from spaceborne hyperspectral UV  
8 measurements: Theory and application, *J. Geophys. Res.*, 115, D00L09,  
9 doi:10.1029/2010JD013982, 2010.

10 Yang, K., Dickerson, R. R., Carn, S. A., Ge, C., and Wang, J.: First observations of SO<sub>2</sub> from the  
11 satellite Suomi NPP OMPS: Widespread air pollution events over China, *Geophys. Res. Lett.*, 40,  
12 4957–4962, doi:10.1002/grl.50952, 2013.

13

14 Zhang, Y., Li, C., Krotkov, N. A., Joiner, J., Fioletov, V., and McLinden, C.: Continuation of long-  
15 term global SO<sub>2</sub> pollution monitoring from OMI to OMPS, *Atmos. Meas. Tech.*, 10, 1495–1509,  
16 <https://doi.org/10.5194/amt-10-1495-2017>, 2017.

17

18

19

20

21

22

23

24

25